Jordan Journal of
PHYSICS
An International Peer-Reviewed Research Journal

Volume 3, No. 1, 2010, 1431 H

Jordan Journal of Physics (*JJP*): An International Peer-Reviewed Research Journal established by the Higher Research Committee, Ministry of Higher Education & Scientific Research, Jordan, and published quarterly by the Deanship of Research & Graduate Studies, Yarmouk University, Irbid, Jordan.

Manuscripts should be submitted to:

Prof. Ibrahim O. Abu Al-Jarayesh
Editor-in-Chief, Jordan Journal of Physics
Deanship of Research and Graduate Studies
Yarmouk University-Irbid-Jordan
Tel. 00 962 2 7211111 Ext. 3735
E-mail: *jjp@yu.edu.jo*
Website: *http://Journals.yu.edu.jo/jjp*

Jordan Journal of
PHYSICS
An International Peer-Reviewed Research Journal

Volume 3, No. 1, 2010, 1431 H

The Hashemite Kingdom of Jordan

Yarmouk University

Jordan Journal of PHYSICS

An International Peer-Reviewed Research Journal

Volume 3, No. 1, 2010, 1431 H

Instructions to Authors

Instructions to authors concerning manuscript organization and format apply to hardcopy submission by mail, and also to electronic online submission via the Journal homepage website (http://jjp.yu.edu.jo).

Manuscript Submission

1- **Hardcopy**: The original and three copies of the manuscript, together with a covering letter from the corresponding author, should be submitted to the Editor-in-Chief:

Professor Ibrahim O. Abu Al-Jarayesh
Editor-in-Chief, Jordan Journal of Physics
Deanship of Scientific Research and Graduate Studies
Yarmouk University, Irbid, Jordan.
Tel: 00962-2-7211111, Ext. 3735
Fax: 00962-2-7211121
E-mail: jjp@yu.edu.jo

2- **Online**: Follow the instructions at the journal homepage website.

Original *Research Articles*, *Communications* and *Technical Notes* are subject to critical review by minimum of two competent referees. Authors are encouraged to suggest names of competent reviewers. *Feature Articles* in active Physics research fields, in which the author's own contribution and its relationship to other work in the field constitute the main body of the article, appear as a result of an invitation from the Editorial Board, and will be so designated. The author of a *Feature Article* will be asked to provide a clear, concise and critical status report of the field as an introduction to the article. *Review Articles* on active and rapidly changing Physics research fields will also be published. Authors of *Review Articles* are encouraged to submit two-page proposals to the Editor-in-Chief for approval. Manuscripts submitted in *Arabic* should be accompanied by an Abstract and Keywords in English.

Organization of the Manuscript

Manuscripts should be typed double spaced on one side of A4 sheets (21.6 x 27.9 cm) with 3.71 cm margins, using Microsoft Word 2000 or a later version thereof. The author should adhere to the following order of presentation: Article Title, Author(s), Full Address and E-mail, Abstract, PACS and Keywords, Main Text, Acknowledgment. Only the first letters of words in the Title, Headings and Subheadings are capitalized. Headings should be in **bold** while subheadings in *italic* fonts.

Title Page: Includes the title of the article, authors' first names, middle initials and surnames and affiliations. The affiliation should comprise the department, institution (university or company), city, zip code and state and should be typed as a footnote to the author's name. The name and complete mailing address, telephone and fax numbers, and e-mail address of the author responsible for correspondence (designated with an asterisk) should also be included for official use. The title should be carefully, concisely and clearly constructed to highlight the emphasis and content of the manuscript, which is very important for information retrieval.

Abstract: A one paragraph abstract not exceeding 200 words is required, which should be arranged to highlight the purpose, methods used, results and major findings**.**

Keywords: A list of 4-6 keywords, which expresses the precise content of the manuscript for indexing purposes, should follow the abstract.

PACS: Authors should supply one or more relevant PACS-2006 classification codes, (available at http://www.aip.org/pacs/pacs06/pacs06-toc.html)

Introduction: Should present the purpose of the submitted work and its relationship to earlier work in the field, but it should not be an extensive review of the literature (e.g., should not exceed 1 ½ typed pages).

Experimental Methods: Should be sufficiently informative to allow competent reproduction of the experimental procedures presented; yet concise enough not to be repetitive of earlier published procedures.

Results: should present the results clearly and concisely.

Discussion: Should be concise and focus on the interpretation of the results.

Conclusion: Should be a brief account of the major findings of the study not exceeding one typed page.

Acknowledgments: Including those for grant and financial support if any, should be typed in one paragraph directly preceding the References.

References: References should be typed double spaced and numbered sequentially in the order in which they are cited in the text. References should be cited in the text by the appropriate Arabic numerals, enclosed in square brackets. Titles of journals are abbreviated according to list of scientific periodicals. The style and punctuation should conform to the following examples:

1. Journal Article:

a) Heisenberg, W., Z. Phys. 49 (1928) 619.
b) Bednorz, J. G. and Müller, K. A., Z. Phys. B64 (1986) 189
c) Bardeen, J., Cooper, L.N. and Schrieffer, J. R., Phys. Rev. 106 (1957) 162.
d) Asad, J. H., Hijjawi, R. S., Sakaji, A. and Khalifeh, J. M., Int. J. Theor. Phys. 44(4) (2005), 3977.

2. Books with Authors, but no Editors:

a) Kittel, C., "Introduction to Solid State Physics", 8th Ed. (John Wiley and Sons, New York, 2005), chapter 16.
b) Chikazumi, S., C. D. Graham, JR, "Physics of Ferromagnetism", 2nd Ed. (Oxford University Press, Oxford, 1997).

3. Books with Authors and Editors:

a) Allen, P. B. "Dynamical Properties of Solids", Ed. (1), G. K. Horton and A. A. Maradudin (North-Holland, Amsterdam, 1980), p137.
b) Chantrell, R. W. and O'Grady, K., "Magnetic Properities of Fine Particles" Eds. J. L. Dormann and D. Fiorani (North-Holland, Amsterdam, 1992), p103.

4. Technical Report:

Purcell, J. "The Superconducting Magnet System for the 12-Foot Bubble Chamber", report ANL/HEP6813, Argonne Natt. Lab., Argonne, III, (1968).

5. Patent:

Bigham, C. B., Schneider, H. R., US patent 3 925 676 (1975).

6. Thesis:

Mahmood, S. H., Ph.D. Thesis, Michigan State University, (1986), USA (Unpublished).

7. Conference or Symposium Proceedings:

Blandin, A. and Lederer, P. Proc. Intern. Conf. on Magnetism, Nottingham (1964), P.71.

8. Internet Source:

Should include authors' names (if any), title, internet website, URL, and date of access.

9. Prepublication online articles (already accepted for publication):

Should include authors' names (if any), title of digital database, database website, URL, and date of access.

For other types of referenced works, provide sufficient information to enable readers to access them.

Tables: Tables should be numbered with Arabic numerals and referred to by number in the Text (e.g., Table 1). Each table should be typed on a separate page with the legend above the table, while explanatory footnotes, which are indicated by superscript lowercase letters, should be typed below the table.

Illustrations: Figures, drawings, diagrams, charts and photographs are to be numbered in a consecutive series of Arabic numerals in the order in which they are cited in the text. Computer-generated illustrations and good-quality digital photographic prints are accepted. They should be black and white originals (not photocopies) provided on separate pages and identified with their corresponding numbers. Actual size graphics should be provided, which need no further manipulation, with lettering (Arial or Helvetica) not smaller than 8 points, lines no thinner than 0.5 point, and each of uniform density. All colors should be removed from graphics except for those graphics to be considered for publication in color. If graphics are to be submitted digitally, they should conform to the following minimum resolution requirements: 1200 dpi for black and white line art, 600 dpi for grayscale art, and 300 dpi for color art. All graphic files must be saved as TIFF images, and all illustrations must be submitted in the actual size at which they should appear in the journal. Note that good quality hardcopy original illustrations are required for both online and mail submissions of manuscripts.

Text Footnotes: The use of text footnotes is to be avoided. When their use is absolutely necessary, they should be typed at the bottom of the page to which they refer, and should be cited in the text by a superscript asterisk or multiples thereof. Place a line above the footnote, so that it is set off from the text.

Supplementary Material: Authors are encouraged to provide all supplementary materials that may facilitate the review process, including any detailed mathematical derivations that may not appear in whole in the manuscript.

Revised Manuscript and Computer Disks

Following the acceptance of a manuscript for publication and the incorporation of all required revisions, authors should submit an original and one more copy of the final disk containing the complete manuscript typed double spaced in Microsoft Word for Windows 2000 or a later version thereof. All graphic files must be saved as PDF, JPG, or TIFF images.

Allen, P.B., "……", in: Horton, G.K., and Muradudin, A. A., (eds.), "Dynamical…….", (North……..), pp….

Reprints

Twenty (20) reprints free of charge are provided to the corresponding author. For orders of more reprints, a reprint order form and prices will be sent with the article proofs, which should be returned directly to the Editor for processing.

Copyright

Disclaimer

Indexing

JJP is currently applying for indexing and abstracting to all related International Services.

Jordan Journal of
PHYSICS
An International Peer-Reviewed Research Journal

Volume 3, No. 1, 2010, 1431 H

Table of Contents:

Volume 3, Number 1, 2010. pp. 1-8

Jordan Journal of Physics

ARTICLE

Study of Black Carbon Levels in City Centers and Industrial Centers in Jordan

K. M. Hamasha[a], **M. S. Almomani**[b], **M. Abu-Allaban**[c] and **W. P. Arnott**[d]

[a] *Department of Physics, Yarmouk University, Irbid, Jordan.*
[b] *Department of Educational Administration and Foundation, Yarmouk University, Irbid, Jordan.*
[c] *Department of Water Management and Environment, Hashemite University, Zarqa, Jordan.*
[a] *Department of Physics, University of Nevada Reno, Nevada, USA.*

Received on: 19/10/2009; Accepted on: 15/3/2010

Abstract: Light absorption coefficients of black carbon (B_{abs}) were measured at several urban and industrial locations in Jordan during the summer of 2007 and the winter of 2008 using the photoacoustic instrument at a wavelength of 870 nm. Black carbon mass concentration (BC) was calculated using B_{abs} . Black carbon levels at urban locations in the summer of 2007 were higher than those obtained at industrial centers. Zarqa had the highest value of BC in summer (29.24μg/m^3) and in winter (13.27μg/m^3). Ibbeen and Irbid city center had relatively high values of BC in winter: 11.75μg/m^3 and 12.48μg/m^3, respectively.

Keywords: Black carbon; Absorption coefficients; Urban air pollution.

Introduction

Jordan is located between 29°10′ N - 33°45′ N and 34°55′ E - 39°20′ E. The discovery of oil in the Arabian Peninsula has resulted in a fast growth and a social and economical development in the Gulf States and their neighboring countries, including Jordan which provides skilled workers. The social and economic development in Jordan has been accompanied by an increase in the consumption of oil for different needs, including residential, commercial, industrial, transportation and power generation. According to figures published by the Department of Statistics (DOS), Jordan imported about six million tons of crude oil in 2005 [1].

Emissions from motor vehicles account for 50–90 percent of air pollution in urban centers [2,3]. There are just over 750,000 vehicles licensed in Jordan, of which 77.5% are registered in the capital, Amman [4]. More than 31% of the vehicles in Jordan are diesel-powered. Vans and trucks represent 33% and 42.7% of the total diesel-powered vehicles, respectively. Most public transportation vehicles work inside cities, especially Amman and Zarqa. Particles emanating from motor vehicles contain sulfate, carbonaceous particles and a large number of chemicals [5].

Other sources of air pollution in Jordan include: power generation which uses heavy oil and natural gas; cement production which uses oil shale; cooking; home furnaces fueled by diesel, natural gas or kerosene; in addition to wood stoves. The unexpected jump in oil prices experienced during the winter of (2007/2008) has forced people with low income in the countryside and mountainous

Corresponding Author: K. M. Hamasha. **Email**: khadeejehh@yahoo.com

areas to switch to wood stoves because they use either olive husk or wood, which are available at low, or no cost in their immediate surroundings.

The negative health impact of air pollution on humans and animals has been widely studied. Findings of several epidemiology studies pointed out that high level of air pollution may result in several health problems, including eye irritation, skin irritation, asthma, lung cancer, cardiovascular problems, high blood pressure, lung tumors and increasing mortality rate [6-10]. Over 300,000 cases of chronic bronchitis, 500,000 asthma attacks and 16 million cases of activity loss recorded in Europe were blamed on vehicle emissions [7]. Exposure to high levels of SO_2 causes the impairment of the respiratory function and aggravates existing respiratory and cardiac illnesses [11]. Long-term exposure to NO_2 lowers the resistance to respiratory infections and aggravates existing chronic respiratory diseases. In addition to its adverse impact on humans, air pollution has adverse impacts on animals and vegetation, in addition to loss of crops.

In spite of the fast growth of urban areas and industrial activities in Jordan, air pollution has not received due attention. Air quality is not routinely monitored anywhere except at Al-Hashemeyyah (located in the Zarqa governorate to the northeast of Zarqa city) which experiences high levels of sulfur oxides and particulates. There have been a few studies that tackled air pollution in Jordan, but they have been limited to three stations only: Downtown and Shmeisani areas in Amman, as well as Al-Hashemeyyah. Those studies have pointed out that local air quality is poor, where concentrations of criteria pollutants (NOx, SOx, CO, PM10, TSP, lead and hydrogen sulfide) exceed the National Air Quality Standards [12,13]. The Jordanian Ministry of Environment has recently launched a project to establish an air quality monitoring network throughout the country, but actual steps towards that goal have not been taken yet.

In light of the above discussion, it is therefore clear that there is a real need to investigate the air pollution problem in Jordan. In this study, air pollution is investigated through measuring black carbon light absorption coefficients at different locations in Jordan. Black carbon, the main constituent of soot, is almost exclusively responsible for aerosol light absorption at long wavelength visible radiation and near infrared wavelengths. This type of pollution is sometimes referred to as black carbon pollution. The exhaust from burning fuels in automobiles, homes and industries is a major source of pollution in the air. Even the burning of wood and charcoal in fireplaces and barbeques can release significant quantities of soot into the air.

Theoretical Background

Black carbon aerosol is a component of air pollution that is emitted by combustion sources including vehicles, especially those with diesel engines. Black carbon and organic carbon are the most efficient light-absorbing aerosol species in the visible spectral range. Organic carbon is strongly wavelength dependent, with increased absorption for UV and short wavelength visible radiation, but hardly at all at 870 nm. Black carbon is very likely to dominate at 870 nm [14-16]. Thus the measurement of aerosol light absorption at wavelengths in the long wavelength visible radiation is correlated to the measurement of black carbon. Light absorption by particles depends on the wavelength of the incident light [17-19]. The relationship between the aerosol absorption coefficient, B_{abs}, and the corresponding black carbon mass concentration (BC) is established by the aerosol specific mass absorption efficiency α_a via the relationship [21]:

$$B_{abs}(Mm^{-1}) = BC(\mu g/m^3) \times \alpha_a(m^2/gm) \qquad (1)$$

The magnitude of α_a ranges from 2 to 20 m^2/g [20]. Black carbon mass concentrations (BC) are calculated from B_{abs} using the light absorption efficiency for black carbon, α_a, such that [21]:

$$BC(\mu g/m^3) = B_{abs}(Mm^{-1}) \,/\, \alpha_a(m^2/gm) \qquad (2)$$

and,

$$\alpha_a = 10 m^2/gm \text{ for } \lambda = 532nm \qquad (3)$$

Since B_{abs} is proportional to $1/\lambda$ [19]; then α_a is also proportional to $1/\lambda$. Therefore,

$$\alpha_a(870nm) = \alpha_a(532nm)(870/532)^{-1} = 6.11 m^2/g \qquad (4)$$

Substituting back in equation (2) yields

$$BC(870nm) = B_{abs}(870nm) / 6.11 \quad (5)$$

Methods

Sampling Sites

Jordan is divided into 12 governorates: Ajlun, Amman, Aqaba, Balqa, Irbid, Jerash, Kerak, Ma'an, Madaba, Mafraq, Tafilah and Zarqa (Figure 1) [22]. Table 1 provides statistics about targeted governorates, including their areas, rural population, urban population and population density [1]. B_{abs} coefficients were measured at selected cities taking into consideration population density, number of motor vehicles, winter heating devices and industrial impact. A summary of the characters of measurement sites is given below:

TABLE 1. Statistics of Jordan governorates according to 2008 estimate [1].

Province	Total Population (2008 est.)	Area (km^2)	Population Density (person/ km^2)	Urban Population (%)	Rural Population (%)
Ajlun	118,496	412	287.1	67.4	32.6
Amman	1,939,405	8231	246.3	91.4	8.6
Balqa	349,580	1076	324.9	63.9	36.1
Irbid	950,700	1621	570.3	76.4	23.6
Zarqa	838,250	4080	205.5	95.3	4.7

FIG. 1. Map of the Governorates of Jordan (from the United States Agency for International Development (USAID) regional website (http://jordan.usaid.gov/images/map1copy.gif.). Retrieved at 4:05 p.m, on 19/10/2008).

Amman

Amman is the capital and the commercial center of Jordan. It spans over an area of nineteen hills. Amman Downtown is characterized by a U-shaped basin surrounded by three mountains. Amman's climate is moderate, where air temperatures range between 20 °C and 30 °C with moderate humidity and frequent westerly breeze for most of the year. Temperatures seldom fall below freezing during winter, which is the rainy season, during which different types of precipitation (rain, snow and frost) take place. There are more than 300,000 motor vehicles (gasoline and diesel) registered in Amman serving 1,140,000 persons [4].

Zarqa

Zarqa is a growing industrial city with a population of about a half million persons (2008 estimate) [1]. It hosts about 35% of the heavy industry in Jordan, including the only oil refinery, an oil-based power plant, steel factories, a pipe factory and a wastewater treatment plant, to mention a few. A total of 2400 industrial activities are registered in the Zarqa Industrial Chamber. Motor vehicles are also a major source of PM_{10}. As a result of such concentrated anthropogenic activities, the air quality in Zarqa is of concern. Residents of Zarqa often complain about odors from the oil refinery and from Alkherbeh Alsamra, where a domestic wastewater treatment plant is located. It is not difficult for travelers passing by Zarqa to notice that there is a real air pollution problem. A clear gray plume emanating from the oil refinery, odors from Alkherbeh Alsamra, in addition to morning haze are easily noticeable in the area.

Information about air pollution in Zarqa is scarce. Few studies were conducted to assess the air quality in the area. The Royal Scientific Society monitored PM_{10} in the area of Al-Hashemeyyah, where most of the Zarqa industries are concentrated. PM_{10} measurements taken by Asi et al. (2001) between March, 2000 and February, 2001 showed that PM_{10} concentrations were higher than the Jordanian 24-hour standard of 120 $\mu g/m^3$ for 20 of the 50 days sampled [12]. No chemical analyses were conducted on the PM_{10} samples collected in that study.

Irbid

Irbid is the second largest city in Jordan. It is located 90 km to the north of Amman on the northern ridge of the Gilead. The population of Irbid is about 650,000 citizens (2008 estimate [1]). Irbid is the center of Irbid Governorate. The city has a bustling community and is a major ground transportation hub between Amman, Syria to the north and Mafraq to the east. No previous attempts were made to assess air quality in Irbid. In addition to motor vehicles, the main source of air pollution during summer, home heating is a potential source of air pollution in winter. Irbid's residents depend on fossil fuels, including kerosene, diesel and natural gas for heating and other household needs.

Ibbeen

Ibbeen is located in Ajlun Governorate. The population of Ibbeen is 8363 inhabitants according to a 2008 estimate [1]. Ibbeen is known for its high altitude, which makes it among the coolest cities in Jordan. Maximum temperatures during January hardly exceed 8.2°C, while minimum temperatures often fall below 0°C. Snow is common in winter, which extends from early November to early May. Several snow storms hit Ibbeen every year, often producing a snow layer as thick as one meter over the highlands in the governorate. The high cost of traditional heating fuel compels people to burn wood, olive cake, agricultural residues and any available combustible materials, including tires. Also, diesel-fueled vehicles (small trucks and mini vans) are very common in Ibbeen.

Fuhais

Fuhais is a city in the Balqa Governorate, situated 15km west of Amman, with about 20,000 residents [1]. Between Amman and Salt (center city of the Balqa Governorate), Fuhais is situated on several freshwater streams that run through the forested area 20 km west of Amman. Fuhais is home to the first constructed cement factory in Jordan, which has been in operation since the fifties of the past century. On several occasions, the factory uses crude oil shale for fuel. People often complain of the environmental problems associated with the factory

activities, which are considered a potential air pollution source in Fuhais. Among the substances which emanate from the factory are soot, sulfur compounds, hydrocarbons, PM10, PM2.5 and TSP, in addition to other carbon compounds. RSS is monitoring TSP and PM10 in Fuhais, but fine particles have not been monitored anywhere in the town.

Sahab

Sahab is an industrial/residential town in Amman Governorate, located 20 km to the south east of Amman, the city. The population of Sahab is about 53,000 residents according to 2008 estimate [1].

Sampling Procedure

A DRI photoacoustic instrument [21] was used at a wavelength of 870 nm to measure the black carbon light absorption coefficients at different locations in Jordan. The experimental procedure is to install the setup of the photoacoustic spectrometer instrument, then collect data. The instrument is controlled by a Labview program. Before installation, the instrument should be located in a well-ventilated area, where the air could be brought in. When it is ready to sample air, the instrument inlet flexible tubing is connected to the inlet of copper tubing, so that an air sample can be pulled in. This copper tubing was fixed to some stable wall with its inlet open all the time during the sampling.

The light absorption measurements were performed approximately every two minutes during the observational periods (from 7:00 am to 6:00 pm) at the selected sites. The selected sites were:

1) The city centers of the three largest cities in Jordan; Amman, Irbid and Zarqa. Measurements at these locations were carried out twice: once in summer 2007 and the other time in winter 2008. The chosen locations for the three cities were close to main streets that have very crowded traffic. The inlet tubing was two meters high from the ground and about three to four meters away from the street.
2) Locations at industrial centers; Jordan Cement Factories at Fuhais, Jordan Petroleum Refinery in Zarqa and Jordan Industrial Estates Corporation at Sahab. Measurements at these locations were conducted in summer 2007. These measurements were made inside the parking lots of these industrial centers.
3) A location in a town that heavily use wood heaters during winter; Ibbeen town center. This measurement was conducted during the winter of 2008. The measurement site was close to the main street (no heavy traffic at this town compared with the three big cities) in the town center.

Since there is just one instrument, and the simultaneous measurements in different cities are impossible, the measurement days were chosen to have very similar weather conditions for each type of measurement (summer and winter measurements).

Table 2 summarizes the results of all the measurements, showing for each location the dates of the measurements, the average black carbon light absorption coefficient for that day ($\overline{B}_{abs}$), the average relative humidity for that day ($\overline{RH}$) and the average temperature for that day ($\overline{T}$).

Results and Discussions

For the summer measurements, $\overline{B}_{abs}$ is higher for the locations in the city centers than for the locations in the industrial centers. Zarqa city center had the highest value of $\overline{B}_{abs}$ (178.68±27.300) Mm^{-1} during a summer day and (81.07±4.860) Mm^{-1} during a winter day. The measured $\overline{B}_{abs}$ at the industrial locations had very low values. A measurement at Ibbeen town center shows that this location had a high value of $\overline{B}_{abs}$ during a winter day.

The BC values calculated using equation (5) are shown in Table 2. As can be learned from Table 2, city centers experience high values of $\overline{B}_{abs}$. Measurements carried out at Zarqa downtown gave the highest levels of black carbon concentration during summer as well as during winter, because of numerous air pollution sources concentrated in the city.

TABLE 2. Measured parameters and measurement locations.

Measurement Location	Date	$\overline{B}_{abs}\,[Mm^{-1}]$	BC[μg/m^3]	$\overline{RH}$ %	$\overline{T}[C^0]$
Irbid City Center	9/7/2007	61.24±2.748	10.02	36.47±0.519	32.25±0.139
Irbid City Center	3/2/2008	76.24±4.430	12.48	86.26±0.317	15.58±0.072
Amman City Center	14/8/2007	67.26±2.418	11.00	30.24±0.640	31.31±0.149
Amman City Center	5/2/2008	22.74±1.666	3.72	68.08±2.63	15.61±0.163
Zarqa City Center	16/8/2007	178.68±27.300	29.24	27.35±0.477	33.00±0.180
Zarqa City Center	27/1/2008	81.07±4.860	13.27	85.75±0.442	19.64±0.338
Ibbeen Town Center/Ajlun	28/2/2008	71.79±8.840	11.75	21.22±0.394	24.85±0.215
Jordan Cement Factories/Fuhais	12/8/2007	7.36±0.564	1.20	31.99±0.432	31.50±0.104
Jordan Industries Estates/Sahab	13/8/2007	13.18±0.969	2.16	30.41±0.433	32.12±0.131
Jordan Petroleum Refinery/Zarqa	15/8/2007	9.7±1.142	1.59	30.24±0.797	29.46±0.265

Measurements performed near industrial complexes indicate low values of black carbon. During summer, $\overline{B}_{abs}$ values were 7.36±0.56 Mm^{-1}, 9.70±1.14 Mm^{-1} and 13.18±0.97 Mm^{-1} at Fuhais Cement Factories, Zarqa Petroleum Refinery and Sahab Industrial Complex, respectively. Low black carbon concentrations in the vicinity of industrial zones are attributed to the efficiency of tall stacks in reducing ground level concentrations of emitted substances. However, tall stacks do not really make air cleaner; they only carry black carbon and other pollutants to distant locations as seen from the results at the location in Zarqa downtown.

Values of $\overline{B}_{abs}$ obtained during winter were 22.74±1.67 Mm^{-1}, 76.24±4.43 Mm^{-1} 81.07±4.86 Mm^{-1} at Amman downtown, Irbid downtown and Zarqa downtown, respectively. It is evident that winter values of $\overline{B}_{abs}$ were lower than summer values at Amman and Zarqa downtowns. Winter value of $\overline{B}_{abs}$ at Irbid downtown was higher than its summer value. Throughout the sampling locations, air temperatures were thirteen to seventeen Celsius degrees lower in winter than in summer, while relative humidity was 38 % to 58% higher. This means that airborne particulates have a better chance to settle down through wet or dry deposition, resulting in lower black carbon concentrations in winter, such as the case in Amman and Zarqa. Higher values of carbon concentration during winter in Irbid indicate that there is a winter-associated source of black carbon. Irbid residents use kerosene heaters, gas heaters, diesel heaters and wood heaters. All of these types of heaters can add a lot of black carbon particles to the environment. In Irbid city, people use more kerosene and wood heaters than other types of heaters. Both types have chimneys outside that could add a lot of black carbon to the air as seen from the measurements on winter days. People in Amman and Zarqa use more gas heaters than other types of heaters. Gas heaters do not have chimneys outsides, and the black carbon released from the incomplete combustion in this type of heaters is normally less than that in the other types of heaters.

As can be learned from Figure 2 and Figure 3, BC increases with population during summer, but the trend is reversed during winter. This is likely due to the fact that people in small towns use primitive heating methods that emit greater amounts of black carbon.

Measurements at Ibbeen town center on a winter day (28/2/2008) show that the city had relatively high levels of black carbon (about 71.79±8.840 Mm^{-1}) for such a small town that is not crowded with automobiles, especially during winter. Ibbeen is very cold in winter, and people usually use wood heaters. These heaters have chimneys outside that release significant amounts of black carbon particles as well as other polluting gases.

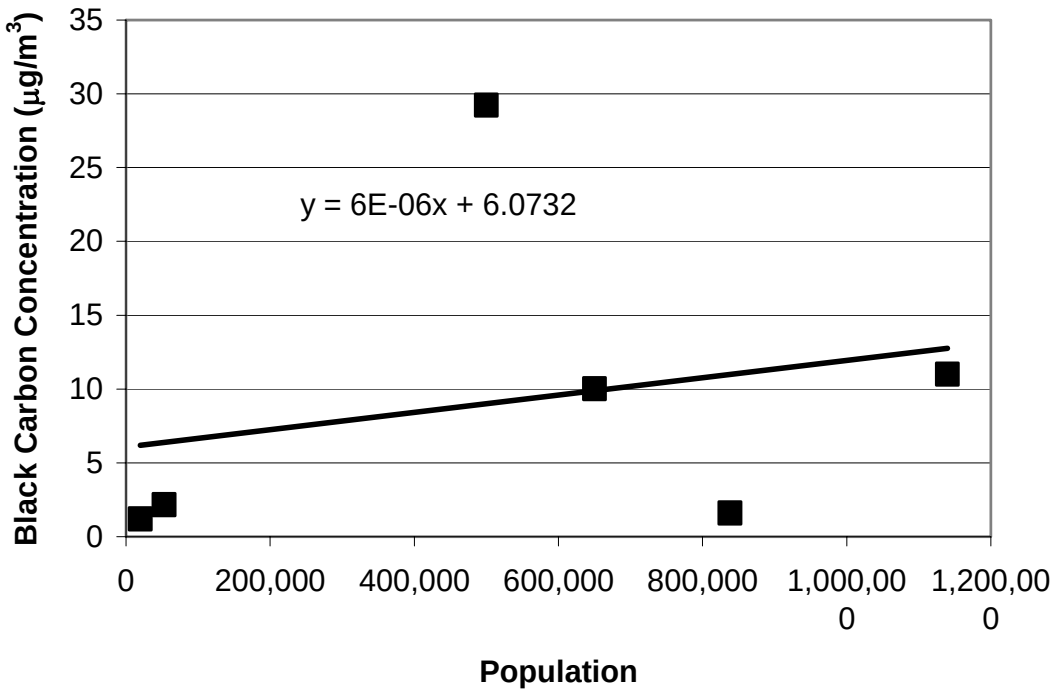

FIG. 2. Dependence of BC on population during summer time.

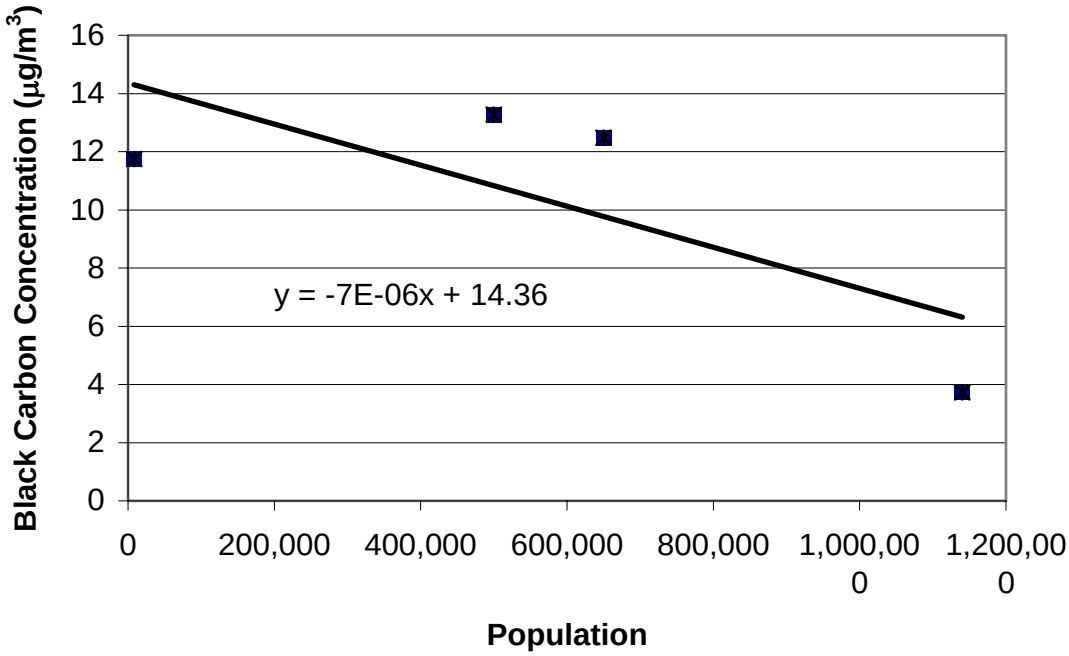

FIG. 3. Dependence of BC on population during winter time.

Conclusions

This study showed that the city of Zarqa had the highest black carbon levels in summer and in winter. Black carbon levels at the sampling sites in industrial centers are the measure of how these centers add the pollutant black carbon to the environment. Measurements in winter showed that black carbon levels are higher at locations where people heavily use wood heaters. In addition to the local impact of this pollutant on the local environmental quality, it also contributes to the global environmental pollution problem.

Acknowledgements

The authors acknowledge the financial support provided by the Deanship of Scientific Research and Graduate Studies at Yarmouk University through grant number 2006/25. Many thanks extend to the Department of Driving and Vehicles Licensing and the Department of Statistics, Amman-Jordan for providing necessary data used in this project.

References

[1]Department of Statistics, Amman, Jordan. http://www.dos.gov.jo/dos_home_a/main/index.htm

[2]Cooper, C.D. and Alley, F.C., Sci. Total Environ. 146/147 (1996) 27.

[3]Gillies, J., Abu-Allaban, M., Gertler, A., Lowenthal, D., Jennison, B. and Goodrich, A. JJEES, 1(1) (2008) 1.

[4]Department of Driving and Vehicles Licensing. Amman, Jordan.

[5]Kassel, R., "Dump Dirty Diesel: The Health and Air Quality Benefits of Cleaner Diesel Engines". Diesel Retrofit Workshop, Oct. 21 (2003).

[6]Pope, C.A., Thun, M.J., Namboodira, M., Dockery, D.W., Evans, J.S., Speizer, F.E. and Health Jr., C.W., American Journal of Respiratory Critical Care Medicine, 151 (1995) 669.

[7]Künzli, N., Kaiser, R., Medina, S., Studnicka, M., Chanel, O., Filliger, P., Herry, M., Horak, F., Puybonnieux-Texier, V., Quénel, P., Schneider, J., Seethaler, R., Vergnaud, J.C. and Sommer, H., The Lancet, 356(9232) (2000) 795.

[8]Pope, C.A, Burnett, R.T., Thun, M.J., Calle, E.E., Krewski, D., Ito, K. and Thurston, G.D., Journal of American Medical Association, 287(9) (2002) 1132.

[9]Takano, H., Yanagisawa, R., Ichinose, T., Sadakane, K., Yoshino, S. and Yoshikawa, T., Am. J. Respir. Crit. Care Med. 165(9) (2002) 1329.

[10]Sanjay, R., "Exposure to Bad Air Raises Blood Pressure", Study Shows. ScienceDaily. (Ohio State University (2008). http://www.sciencedaily.com /releases/2008/07/080728114026.htm

[11]Andre, N.E., Diaz-Sanchez, D. and Li, N., Current Opinion in Pulmonary Medicine, 7(1) (2001) 20.

[12]Asi, R., Anani, F. and Asswaeir, J. "Studying Air Quality in Al-Hashemeyyah Area/Zarqa". A report prepared by the Royal Scientific Society (RSS) for the general institution for the protection of the environment, Amman, Jordan, (2001).

[13]Hamdi, M.R., Bdour, A. and Tarawneh, Z. Environmental Engineering Science, 25(9) (2008) 1333.

[14]Rosen, H., Hansen, A. D. A., Gundel, L. and Novakov, T., Applied Optics, 17 (1978) 3859.

[15]Lindberg, J.D., Douglass, R.E. and Garvey, D.M. Applied Optics, 32 (1993) 6077.

[16]Lewis, K., Arnott, W.P., Moosmüller, H. and Wold, E., Journal of Geophysical Research, 113 (2008) D16203.

[17]Moosmüller, H., Arnott, W.P., Rogers, C.F., Chow, J.C., Frazier, C.A., Sherman, L.E. and Dietrich, D.L., J. Geophysics. Res., 103(D21) (1998) 28149.

[18]Horvath, H., Catlan, L. and Trier, A., Atmos. Environ. 31(22) (1997) 3737.

[19]Kirchstetter, T.W., Novakov, T. and Hobbs, P.V., J. Geophysics. Res. 109(D21) (2004) D21208.

[20]Liousse, C., Cachier, H. and Jennings, S.G., Atmospheric Environment, 27A, (1993) 1203.

[21]Arnott, W.P., Moosmüller, H., Rogers, C.F., Jin, T. and Bruch, R., Atmospheric Environment, 33 (1999) 2845.

[22]United States Agency for International Development (USAID) (http://jordan.usaid.gov/images/map1copy.gif.). Retrieved at 4:05 p.m. on 19/10/2008).

Volume 3, Number 1, 2010. pp. 9-15

Jordan Journal of Physics

ARTICLE

Non-Dissociative Single-Electron Capture Studied for O_2^{2+} Ions on Ar, N_2 and He at 100 eV

Osama A. Abu-Haija

Applied Physics Department, Tafila Technical University, P. O. Box 179, Zip Code 66110, Tafila-Jordan.

Received on: 15/2/2010; Accepted on: 13/5/2010

Abstract: Energy-gain spectra for single-electron capture by O_2^{2+} ions colliding with Ar, He and N_2 have been measured at an impact energy of 100 eV and 0º scattering angle by means of translational energy-gain spectroscopy. In O_2^{2+} - Ar and N_2 collisions, only one peak is observed at the energy-gain around 3.5 eV, which is correlated with non-dissociative single-electron capture from ground state (X $^1\Sigma_g^+$) of O_2^{2+} ions into the A $^2\Pi_u$ state of O_2^+. However, for the O_2^{2+} - He collision system, the dominant channels are due to capture into the ground state X $^2\Pi_g$ of O_2^+ from W $^3\Delta_u$, B $^3\Pi_g$ and B$^{/}$ $^3\Sigma_u^-$ metastable states of the O_2^{2+}, respectively. A reasonable description of the dominant final states is obtained qualitatively in terms of the reaction windows, which are calculated using the Landau-Zener (LZ) model and the extended version of the classical over-the-barrier (ECOB) model. Differential cross sections for single-electron capture by 100 eV O_2^{2+} ions from Ar have also been measured. The results are quantitatively explained by semi-classical model based on Coulomb potential energy curves.

Keywords: Single-electron capture; Non-dissociative electron capture; Reaction window.

Introduction

Experimental and theoretical investigations of electron capture processes occurring in collisions between doubly charged molecular ions and atomic/molecular targets have recently received considerable attention. The need to understand ion-atom/molecule collision processes is important in a number of applications, such as: material science, plasma science -where low temperature plasmas play a key role in determining characteristics of target materials and of plasma behavior- and astrophysics. Also, atmospheric molecular ions (O_2^+, N_2^+, CO^+ and CO_2^+) are important constituents of the earth's upper atmosphere. Information on mechanisms responsible for their excitation is crucial to a complete understanding of atmospheric phenomena [1-4]. Single-electron capture by doubly charged molecular ion O_2^{2+} from atomic targets has been studied previously in the keV region [5]. However, in the case of molecular targets, the only experimental measurement at low-energy collisions has been recently made by Kamber [6]. In his work, the translational energy-gain spectroscopy technique has been used to measure the energy gain spectra of 100 eV O_2^{2+} ions with O_2 and Ne at different scattering angles.

Presented herein are energy-gain spectra for state-selective non-dissociative single-electron capture in collisions of O_2^{2+} recoil ions with N_2, Ar and He targets at a laboratory impact energy of 100 eV and 0° scattering angle.

The present measurements were performed on a differential energy

Corresponding Author: O. Abu-Haija. **Email**: oabuhaija@ttu.edu.jo

spectrometer, which has been fully described previously [7]. Briefly, doubly molecular oxygen ions were produced in a recoil ion source from oxygen molecules by using 25 MeV F^{4+} ions from the Western Michigan University tandem Van de Graaff accelerator as a pump beam. After being mass analyzed by a 180° double-focusing magnet, the ions were guided with the aid of horizontal and vertical parallel deflection plates into the entrance of a gas cell containing a low-pressure target gas. The projectile ions that had undergone capture were energy analyzed by means of a 90° double-focusing electrostatic analyzer (ESA). These ions were scattered through a nominal angle θ into a solid angle ($\Delta\Omega$) of about 3 x 10^{-3} sr. The scattering angle θ is selected by means of an aperture located in front of the ESA. The analyzed ions were then detected by a one-dimensional position sensitive channel-plate detector located at the focal plane of the ESA.

Results and Discussion

When doubly charged molecular oxygen ions collide with atomic/molecular targets, a variety of reaction channels is possible through which electron capture may take place. Non-dissociative single-electron capture has been found the most probable event as a result of low-energy ion-atom/molecule collisions. This process of charge transfer, by which an electron from a neutral target is captured to a doubly charged ion, can be presented by the expression:

$$O_2^{2+} + X \rightarrow O_2^{+} + X^{+} + Q, \qquad (1)$$

where Q is the energy gained by the projectile ion during the collision. In classical two-body dynamics, the energy gained by the projectile ion during a collision can be expressed as the difference between the final kinetic energy E_f of the scattered projectile ion and the initial kinetic energy E_0 of the incident projectile ion, $Q = E_f - E_0$. However, the relationship of the energy gain Q to the energy defect ΔE, which is defined as the difference in the binding energies of the collision products, is found to be [8]:

$$Q = \Delta E - \Delta K \qquad (2)$$

where ΔK, defined below, is the translational energy given to the target and ΔE is calculated from spectroscopic data according to the following formula:

$$\Delta E = I_p(O_2^{+}) - I_p(X) - E_x, \qquad (3)$$

where $I_p(O_2^{+})$ and $I_p(X)$ are, respectively, the ionization energies of the projectile product ion (O_2^{+}) and the target atom/molecule X, with the target atom/molecule being assumed to be in its ground electronic state and the captured electron being in the most loosely bound orbital and E_x is the excitation energy of the xth level of the projectile product ion (O_2^{+}) or the target product ion X^{+}. The general expression of the translational energy ΔK given to the target is given by [9]:

$$\left.\begin{aligned}\Delta K = {} & \frac{M}{M+m}\left(1-\cos\theta\right)\left[\frac{2mE_0}{M+m} - \Delta E\right] \\ & + \frac{M\left(\Delta E\right)^2}{4mE_0}\cos\theta\end{aligned}\right\}, \qquad (4)$$

where M and m are, respectively, the projectile and target masses, E_0 is the laboratory translational energy of the projectile and θ is the laboratory scattering angle of the projectile. It should be pointed out that for these collision systems, the calculated values of ΔK are very small and can be neglected, giving $Q = \Delta E$. Therefore, the energy spectra are expressed in terms of the Q values. The energy levels for O_2^{2+} and O_2^{+} ions used in calculating the energy defect of the reaction were taken from published tables [10-14].

The reaction channels observed in the measured energy gain spectra have been labeled according to the notation previously described by Kamber et al. [15]. The designations I, II and III represent, respectively, the ground, first and second electronically excited states of O_2^{2+}; α, β and γ represent the ground and subsequent electronically excited states of O_2^{+} ion; X represents the ground state of the target product (see Table 1). In the following sections, the results for single-electron capture processes in collisions of O_2^{2+} ions with Ar, N_2 and He are presented and discussed.

TABLE 1. Description and nomenclature of O_2 ionic states and ionized target states.

Projectile O_2^{2+}		O_2^+ Products		Target Products	
State	Symbol	State	Symbol	State	Symbol
$X\ ^1\Sigma_g^+$	I	$X\ ^2\Pi_g$	α	$Ar^+ (3p^5\ ^2P^o_{3/2})$	X
$A\ ^3\Sigma_u^+$	II	$a\ ^4\Pi_u$	β	$Ar^+ (3p^6\ ^2S_{1/2})$	A
$W\ ^3\Delta_u$	III	$A\ ^2\Pi_u$	γ	$N_2^+ (^2\Sigma_g^+)$	X
$B\ ^3\Pi_g$	IV	$b\ ^4\Sigma_g^-$	δ	$N_2^+ (^2\Pi_u)$	A
$B'\ ^3\Sigma_u^-$	V	$B\ ^2\Sigma_g^-$	ε	$He^+ (1s\ ^2S_{1/2})$	X
$1\ ^3\Delta_g$	VI	$C\ ^4\Sigma_u^-$	ζ	$He^+ (2p)$	A

Sources: [10-14].

I. O_2^{2+} + Ar Collisions

Fig. 1 shows the translational energy-gain spectra obtained for single-electron capture by 100 eV O_2^{2+} ions from Ar at different scattering angles. At 0° scattering angle, only one peak is clearly seen at energy-gain around 3.5 eV. This peak is correlated with non-dissociative single-electron capture reaction channel from the ground state of ($X\ ^1\Sigma_g^+$) of O_2^{2+} ions into the $A\ ^2\Pi_u$ state of O_2^+. There are smaller contributions due to capture into the $B\ ^2\Sigma_g^-$ and $b\ ^4\Sigma_g^-$ states of O_2^+ from the low-lying metastable state $A\ ^3\Sigma_u^-$ of the O_2^{2+} ions via reaction channels IIεX and IIδX. It is of interest to compare our data with the earlier spectrum of Hamdan and Brenton [5]. The spectrum was measured at O_2^{2+} incident energy of 6 keV. Their measurements disagree with the present results for which the dominant peak was observed to be due to electron capture by O_2^{2+} ($A\ ^3\Sigma_u^+$) excited state. This is attributed to the high collision energy they used in their measurements, since the reaction window depends modestly on the collision energy.

As the scattering angle is increased, the IγX channel remains dominant and contributions from reaction channel IIεX and IIδX remain the same with increasing the scattering angle. At a scattering angle of 1.87º, peak IγX is observed to be shifted toward a larger Q-value due to the populations of different vibrational states of the $A\ ^2\Pi_u$ state of O_2^+. The amount of the energy given to the target in this collision system is very small (less than 0.1 eV, see equation (4)). Also shown are our calculated reaction windows, the range of Q values where the probability for single-electron capture is large, using both a single-crossing Landau-Zener (LZ) model [16-18] and the extended version of the classical over-the-barrier (ECOB) model [19]. Calculated peak values have been normalized to our observed peak values in the energy spectrum. The reaction window based on a single-crossing LZ model predicts the IγX channel to be the dominant process, since its Q value lies very close to the maximum of the reaction window. The reaction window based on a single-crossing ECOB model accommodates the IγX channel and favors larger Q values compared to the dominant channel.

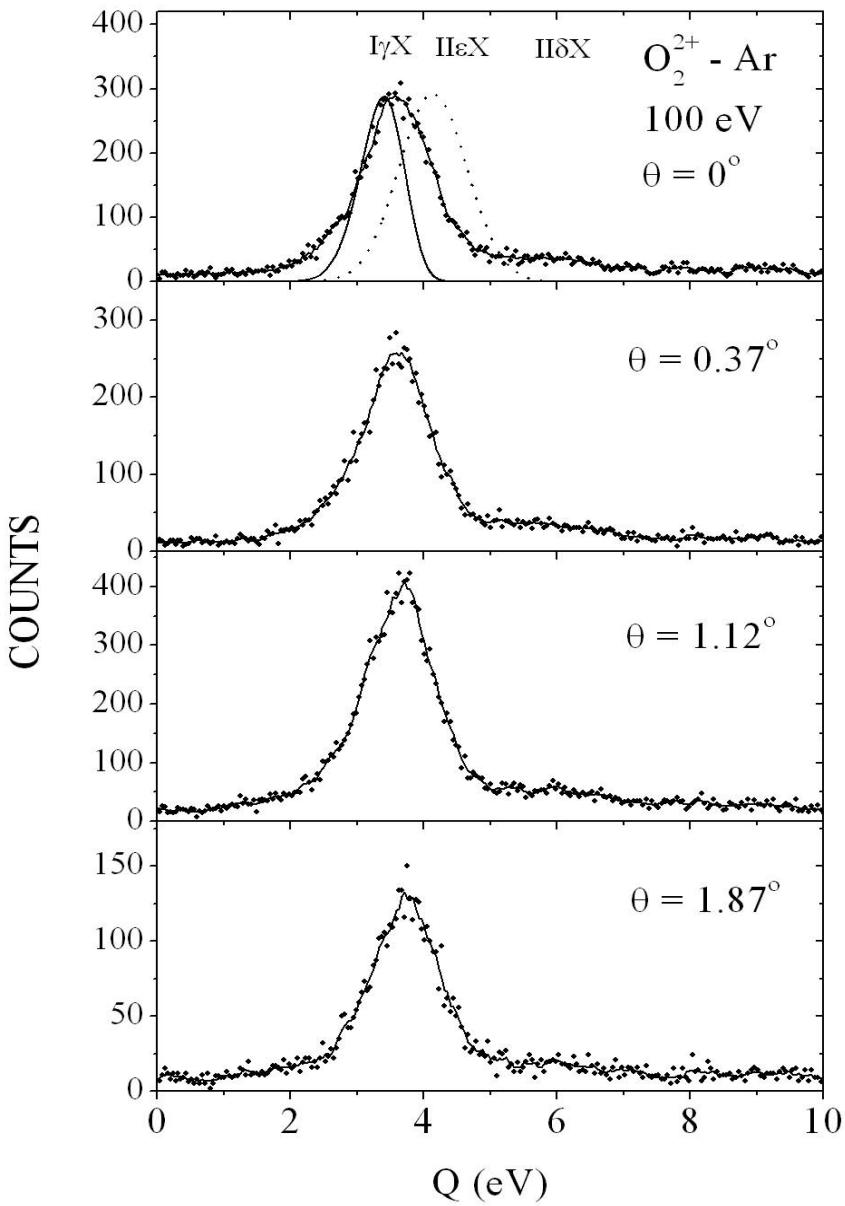

FIG. 1. Translational energy-gain spectra for single-electron capture by 100 eV O_2^{2+} ions from Ar at different projectile laboratory scattering angles. Also shown are reaction windows calculated on the basis of a single-crossing LZ model (full curve) and the ECOB model (dashed curve). Smooth lines are drawn to guide the eye.

The experimental differential cross sections ($d\sigma/d\Omega$) for single-electron capture by 100 eV O_2^{2+} ions from Ar were found using the translational energy-gain technique, by calculating the area under the peaks (total intensity) in the energy-gain spectra at different projectile laboratory scattering angles using curve fitting program. The general features of the distributions are qualitatively explained in terms of a semi-classical model based on Coulomb potential curves [20]. The traditional two-state model has been used to estimate the critical angle θ_c, which corresponds to capture at an impact parameter equal to the crossing radius, by assuming that capture occurs at a localized curve crossing between the potential energy curves for entrance and exit channels. For small laboratory scattering angles, $\theta_c = Q/2E_0$, where Q is the exoergicity of the collision and E_0 is the laboratory impact energy. This angle separates the events scattered at smaller angles due to capture on the way-out and events scattered at larger angles due to capture on the way-into the collision. The experimental differential cross sections and the theoretical calculations folded with the

experimental resolution are shown in Fig. 2. The value of the largest calculated cross section has been normalized to the experimental value of the peak observed in the spectrum. The calculation is performed assuming that capture through IγX channel is the only dominant reaction channel with the IIεX channel strongly promoting the entrance channel. The experimental data show a forward peak inside the critical angle θ_c = 1.01°, which corresponds to the IγX capture channel. The forward peak clearly represents contributions from electron capture that takes place on the way-out of the collision. The calculated distribution shows a peak lying near θ_c and underestimates the contribution from capture on the way-out of the collision.

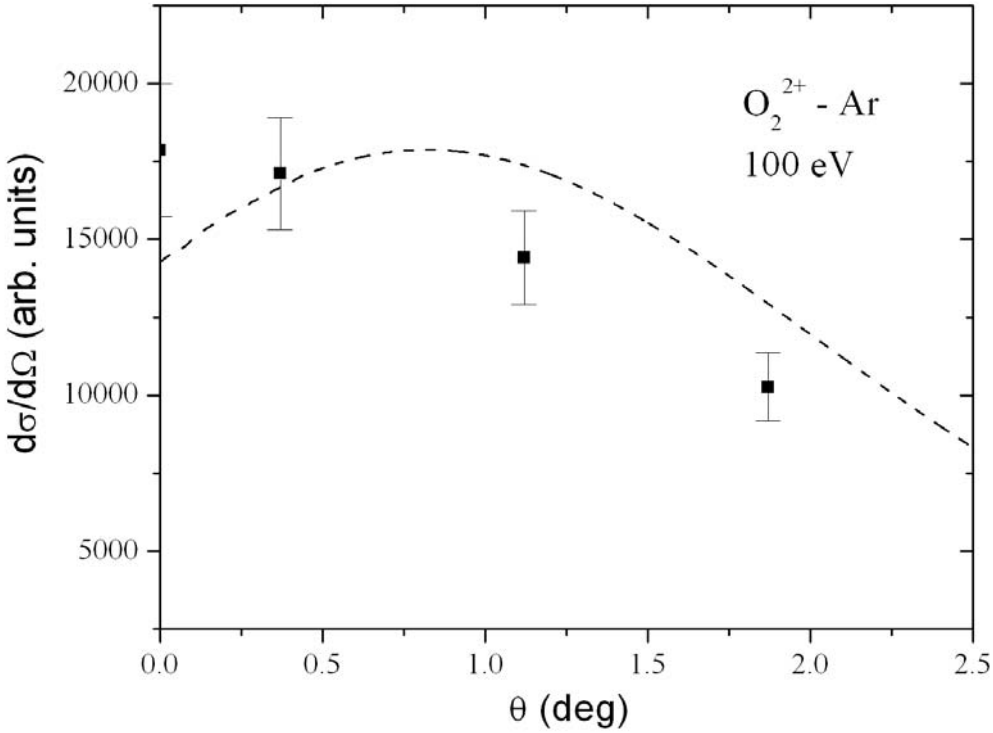

FIG. 2. Experimental and calculated differential cross sections (dσ/dΩ) for single-electron capture by 100 eV O_2^{2+} ions from Ar. ■, present results; the broken curve is the theoretical calculation folded with experimental resolution.

II. O_2^{2+} + N_2 Collisions

Fig. 3 shows the translational energy-gain spectrum obtained for single-electron capture by O_2^{2+} ions from N_2 at zero-degree scattering angle. The shape and the peak position are almost the same as those for the Ar target. The peak in the spectrum is due to the non-dissociative single-electron capture from the ground state of (X $^1\Sigma_g^+$) of incident ions into the A $^2\Pi_u$ state of O_2^+. The reaction channel IγX is positioned near the center of the reaction windows based on the ECOB model and LZ model. Both reaction windows accommodate most of the observed features in the spectrum.

III. O_2^{2+} + He Collisions

Fig. 4 shows the translational energy-gain spectrum for the formation of O_2^+ ions from the reaction of 100 eV O_2^{2+} ions with He at zero-degree projectile scattering angle. The spectrum shows only one peak centered at about 5.8 eV. This peak correlates with non-dissociative single-electron capture into the ground state X $^2\Pi_g$ of O_2^+ from W $^3\Delta_u$, B $^3\Pi_g$ and B$^/$ $^3\Sigma_u^-$ metastable states of the O_2^{2+}, respectively. Again, the comparison with the results of Hamdan and Brenton [5] at 6 keV impact energy shows good agreement with the present measurements. The reaction window based on a single-crossing LZ model favors Q values smaller than those observed and is positioned near the dominant reaction channel IIαX, while the reaction window based on the ECOB model provides the best description of the observed spectrum.

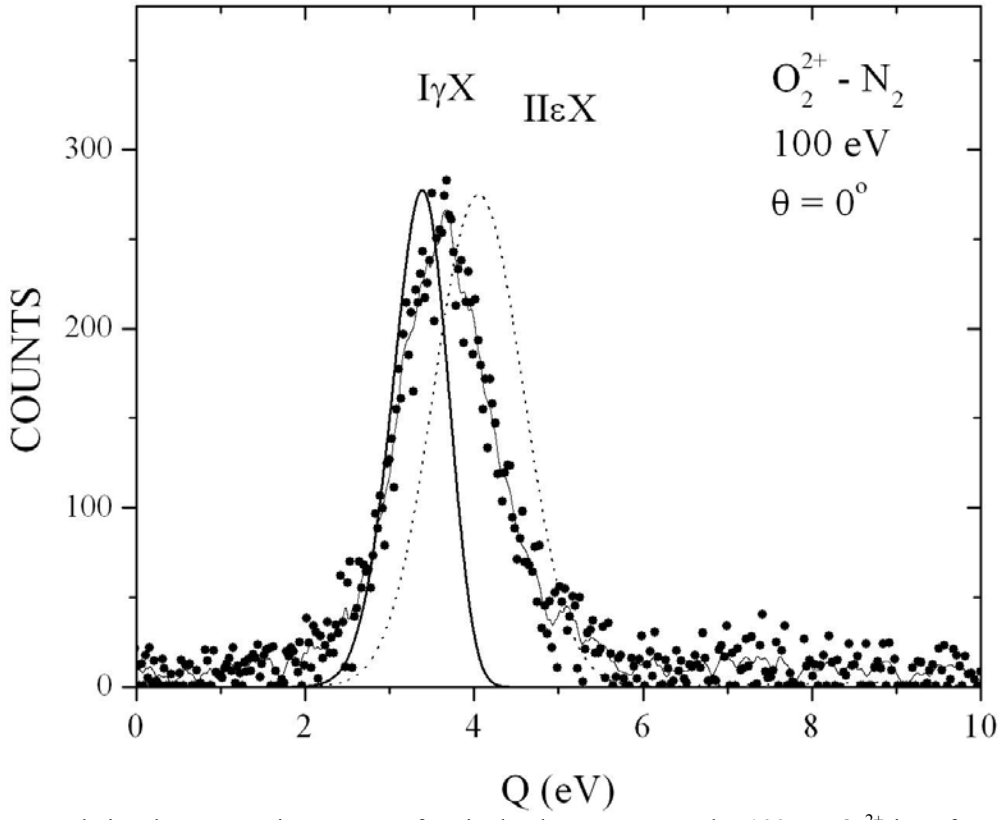

FIG. 3. Translational energy-gain spectrum for single-electron capture by 100 eV O_2^{2+} ions from N_2 at zero-degree projectile laboratory scattering angle. Also shown are reaction windows calculated on the basis of LZ model (full curve) and the ECOB model (dashed curve). Smooth line is drawn to guide the eye.

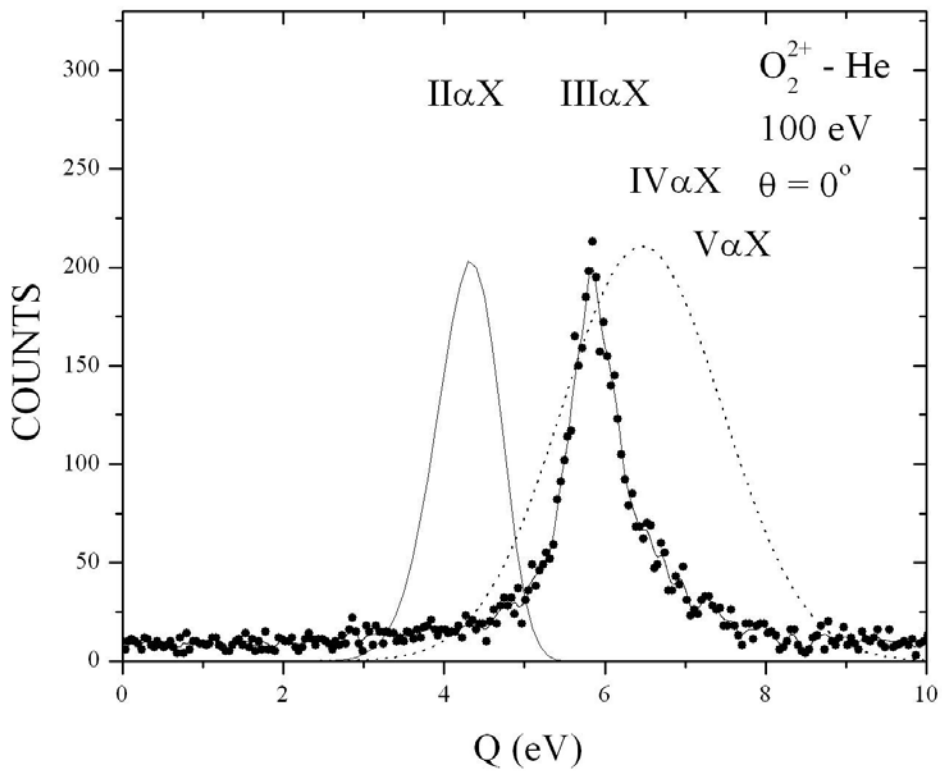

FIG. 4. Translational energy-gain spectrum for single-electron capture by 100 eV O_2^{2+} ions from He at zero-degree projectile laboratory scattering angle. Also shown are reaction windows calculated on the basis of LZ model (full curve) and the ECOB model (dashed curve). Smooth line is drawn to guide the eye.

It is interesting to note that the Q-scale distribution of translational energy gain for single-electron capture by 100 eV O_2^{2+} ions from Ar and N_2 appear Gaussian whereas the distribution from He is Pearson or Lorentzian in shape. This is probably due to the fact that for Ar or N_2, only one reaction channel contributes to the capture process, while for the He target, more than one channel contribute to the capture process.

Conclusion

The main objective of the present investigation has been to study single-electron capture in low-energy collisions of O_2^{2+} ions with Ar, N_2 and He by means of translational energy-gain spectroscopy. Translational energy-gain spectra for single-electron capture by O_2^{2+} ions from Ar and N_2 indicated that the dominant reaction channels were correlated with non-dissociative single-electron capture from the ground state (X $^1\Sigma_g^+$) of O_2^{2+} ions into the A $^2\Pi_u$ state of O_2^+, while for He target the dominant channel is due to capture into the ground state X $^2\Pi_g$ of O_2^+ from W $^3\Delta_u$, B $^3\Pi_g$ and B$^{/}$ $^3\Sigma_u^-$ metastable states of the O_2^{2+}, respectively. The energy-gain spectra were interpreted qualitatively in terms of the reaction windows, which are calculated using the single-crossing LZ model and the ECOB model. The reaction windows based on the ECOB model provide the best description of the observed spectra.

Acknowledgements

The author wishes to express his gratitude for the kind hospitality extended to him during his stay (summer 2009) at Western Michigan University, where this work was performed. I am indebted to Prof. E.Y. Kamber (Western Michigan University) for many fruitful discussions and friendly assistance. This work was supported in part by a research grant Tafila Technical University.

References

[1]Mathur, D., Phys. Rep. 225 (1993) 193.

[2]Cravens, T.E., Geophys. Res. Lett. 24 (1997) 105.

[3]Wargelin, J.B. and Dark, J.J., Astrophys. J. 546 (2001) L57.

[4]Pequignot, D., Astronomy and Astrophysics, 81 (1980) 356.

[5]Hamdan, M. and Brenton, A.G., Chem. Phys. Lett. 164 (1989) 413.

[6]Kamber, E.Y., Journal of Physics: Conference Series 163 (2009) 012066.

[7]Yaltkaya, S., Kamber, E.Y. and Ferguson, S.M., Phys. Rev. A, 48 (1993) 382.

[8]Kamber, E.Y. and Cocke, C.L., Springer Series in Chemical Physics, 54 (1991) 91.

[9]Cooks, R.G., "Collision Spectroscopy", (Plenum Press, New York, 1978).

[10]Turner, D.W., Baker, A.D., Baker, C. and Brundle, C.R., "Molecular Photoelectron Spectroscopy", (Wiley, London, 1970).

[11]WWW homepage of the NIST Atomic Spectra Database (http://physics.nist.gov/).

[12]Leputsch, P., Dumitriu, F., Aumayr, F. and Winter, H.P., J. Phys. B, 30 (1997) 5009.

[13]Wetmore, R.W. and Boyd, R.K., J. Chem. Phys. 90 (1986) 5540.

[14]Koslowski, H.R., Lebius, H., Staemmier, V., Wiesemann, K. and Huber, B.A., J. Phys. B, 24 (1991) 5023.

[15]Kamber, E.Y., Mathur, D. and Hasted, J.B., J. Phys. B, 16 (1982) 3025.

[16]Landau, L.D., Phys. Z. Sowjetunion, 2 (1932) 46.

[17]Zener, C., Proc. R. Soc. London Ser. A, 137 (1932) 696.

[18]Oslon, R.E. and Salop, A., Phys. Rev. A, 14 (1976) 579.

[19]Niehaus, A., J. Phys. B, 19 (1986) 2925.

[20]Anderson, L.R., Danared, H. and Barany, A., Nucl. Instrum. Meth. Phys. B, 23 (1987) 54.

Volume 3, Number 1, 2010. pp. 17-24

Jordan Journal of Physics

ARTICLE

Effect of Magnetic Anisotropy on a One - Dimensional System of Magnetic Particles

M. A. Gharaibeh[a], **A. A. Obeidat**[a], **D.H. Al-Samarh**[a], **M. K. Qaseer**[a] and **N.Y. Ayoub**[b]

[a] *Physics Department, Jordan University of Science and Technology, Irbid, Jordan.*
[b] *Physics Department, Yarmouk University, Irbid, Jordan.*

Received on: 23/3/2010; Accepted on: 8/6/2010

Abstract: Using a statistical approach, the magnetization and the initial susceptibility for a one – dimensional chain of a dilute ferromagnetic fluid have been investigated. Our assembly consisted of an *N* – particle chain with *N/3* non - interacting systems. We have studied three distinct cases: case 1 with randomly oriented easy axis of the particle assembly and the applied magnetic field is parallel to the chain. We found that the initial susceptibility follows Curie – Weiss behavior with positive ordering temperature T_o that does not depend on the anisotropy constant *K* of the particles. In case 2, the applied field is perpendicular to the chain with randomly oriented easy axis. In this case, we found an antiferromagnetic transition with no dependence on *K*. In case 3, when the easy axis is fixed at an angle ξ relative to *H*, we found that whether *H* parallel or perpendicular to the chain there is an interplay between ferromagnetic-like and antiferromagnetic-like behavior, depending on *K*, particle separation within the system and the angle ξ.

PACS: 75.30.Gw, 47.65.Cb, 75.50.Gg, 75.50.Ee
Keywords: Magnetic anisotropy; Ferromagnetism; Antiferromagnetism; Ferrofluid.

Introduction

Many scientists have been interested in studying the magnetic behavior of the magnetic fine particle systems in liquid and solid states [1–4]. Many different models have been introduced to study the magnetic behavior analytically or numerically. Morup [5] showed that the magnetic interaction leads to spontaneous ordering, and he was able to give a good description of the magnetic properties above the ordering temperature. The effect of orientation texture has been considered analytically by Chantrell *et al.* [6] and numerically be Raikher [7]. Odeh *et al.* [8] used the Dimer model and found that the magnetic behavior of ferro-fluids depends on the direction of the external magnetic field with respect to the particle chain. Ayoub *et al.* [9] suggested interactions other than the dipole – dipole interaction to explain the Curie – Weiss behavior for a three - dimensional Dimer model. Smirnov and Komogortsev [10] used the generalized SW model [11, 12] in order to numerically investigate the magnetization curves of an ensemble of randomly oriented ferromagnetic single-domain nanoparticles. They discussed the possibility of estimating the ratio of the uniaxial anisotropy energy to the total magnetic anisotropy energy at low fields. For the case of transition between different symmetries of local magnetic anisotropy energy, they suggested that a more complicated form of nonlinear variations of the magnetic properties must be considered. A hint of possible ferromagnetic transition was shown experimentally by Mamiya *et al.* [13]. They have conducted their experiments

Corresponding Author: M. A. Gharaibeh. **Email**: magh@just.edu.jo

on strongly interacting Fe_3N ferrofluids. Magnetic properties of two-dimensional layers of interacting nanoparticles with random anisotropy were calculated using Monte Carlo simulations [14]. The model refers to thin granular antiferromagnetic films. The effect of shape anisotropy on magnetic properties of ferrofluids has been calculated [15]. Two particle interactions were considered, and it was found that the anisotropy plays a major role in determining the magnetic state.

In this paper, we will use a statistical mechanical approach to investigate the effect of anisotropy energy dominated by the dipole – dipole interaction on the initial susceptibility of a ferro-fluid chain. We will consider an assembly consisting of *N* single domain fine magnetic particles constrained to move in one dimension. We will propose a three particle interaction that we shall call the Trimer model. In the Trimer model, the particles are approximated to a set of *N/3* independent systems. Each system consists of three interacting identical spherical particles. Each particle has an average magnetic dipole moment μ which is randomly oriented and each particle has an easy axis. We will investigate three distinct configurations. The first two are with randomized easy axis and applied field *H* parallel or perpendicular to the assembly. The last case is with a fixed orientation of the easy axis and *H* parallel or perpendicular to the assembly. The first two cases are applicable for the ferromagnetic fluids, while the third is applicable for a solid matrix.

Results and Discussion

Consider an assembly of *N/3* systems; the total partition function is given by:

$$Z_T = \frac{Z^{N/3}}{\left(N/3\right)!} , \qquad (1)$$

where *Z* is the partition function for a single system. A single system is consisting of three interacting particles. The single system partition function is given by:

$$Z = \int \mathrm{Exp}[-\frac{E_T}{k_B T}]\ \mathrm{d}\Gamma . \qquad (2)$$

The integral is to be taken over the volume phase space $\mathrm{d}\Gamma$. The total energy E_T of our system can be represented as:

$$E_T = E_0 + E_{p-p} + E_a , \qquad (3)$$

where E_0 is the external field dipole interaction energy, E_{p-p} is the total dipole – dipole interaction energy among the particles of a single system and E_a is the anisotropic energy of the system. The external energy is given by:

$$\left.\begin{aligned} E_0 &= -\sum_1^3 \vec{\mu}_i \cdot \vec{H} \\ &= -\mu H \left(\cos\theta_1 + \cos\theta_2 + \cos\theta_3\right) \end{aligned}\right\}, \qquad (4)$$

where θ_i is the angle between the direction of the external applied magnetic field *H* and the magnetic dipole moment of each particle within the single system. The dipole – dipole interaction energy is given by:

$$E_{p-p} = \sum_{i>j}^{3}\sum_{j=1}^{3} \frac{\vec{\mu}_i \cdot \vec{\mu}_j - 3(\hat{r}_{ij} \cdot \vec{\mu}_i)(\hat{r}_{ij} \cdot \vec{\mu}_j)}{r_{ij}^3} , \qquad (5)$$

where μ_i and μ_j are the dipole moments of particle *i* and particle *j*, respectively and r_{ij} is the separation between the two particles. The anisotropy energy is given by:

$$E_a = KV\sum_{i=1}^{3}\sin^2\beta_i , \qquad (6)$$

where *K*, *V* and β_i are, respectively, the anisotropy constant, the volume of each particle and the angle between the magnetic dipole moment of the particle and its easy axis.

The magnetization M of the system can be calculated using the equation:

$$M = \frac{Nk_B T}{3Z}\frac{\partial Z}{\partial H} . \qquad (7)$$

The initial susceptibility of the system can be calculated as:

$$\chi = \lim_{H\to 0}\frac{\partial M}{\partial H} . \qquad (8)$$

Now, we will discuss in detail each of the three cases mentioned above. We will use

Eq.7 to calculate the magnetization and Eq. 8 to calculate the susceptibility.

Parallel Configuration

In this case the applied magnetic field is parallel to the chain axis (Fig. 1). In the limit that the particle – particle interaction energy and the anisotropy energy are very small, one can expand the exponential term in the partition function as:

$$Z = e^{\frac{3KV}{k_B T}} \int \mathrm{Exp}\left[\frac{\mu H}{k_B T}\left(\cos\theta_1 + \cos\theta_2 + \cos\theta_3\right)\right]$$
$$\times\left\{1 + \frac{\mu^2}{k_B T}\left(\frac{g_1}{x_1^3} + \frac{g_2}{x_2^3} + \frac{g_3}{(x_2 - x_1)^3}\right) + \frac{KV}{k_B T}\left(J_1^2 + J_2^2 + J_3^2\right)\right. \tag{9}$$
$$\left. + \frac{1}{2}\left(\frac{\mu^2}{k_B T}\left(\frac{g_1}{x_1^3} + \frac{g_2}{x_2^3} + \frac{g_3}{(x_2 - x_1)^3}\right) + \frac{KV}{k_B T}\left(J_1^2 + J_2^2 + J_3^2\right)\right)^2\right\} \mathrm{d}\Gamma$$

where

$$\begin{aligned} g_1(\theta_1,\theta_2,\varphi_1,\varphi_2) &= 2\cos\theta_1\cos\theta_2 - \sin\theta_1\sin\theta_2\cos(\varphi_1 - \varphi_2) \\ g_2(\theta_1,\theta_3,\varphi_1,\varphi_3) &= 2\cos\theta_1\cos\theta_3 - \sin\theta_1\sin\theta_3\cos(\varphi_1 - \varphi_3) \\ g_3(\theta_2,\theta_3,\varphi_2,\varphi_3) &= 2\cos\theta_2\cos\theta_3 - \sin\theta_2\sin\theta_3\cos(\varphi_2 - \varphi_3) \\ J_i &= \cos\beta_i = \cos\theta_i\cos\eta_i + \sin\theta_i\sin\eta_i\cos(\varphi_i - \psi_i) \end{aligned} \tag{10}$$

In Eq. 9, x_1 is the separation between the first and the second particles, while x_2 is the separation between the first and the third particles. Performing the necessary calculations, the initial susceptibility for the system in the limit $\alpha = \frac{\mu H}{k_B T} < 1$ is obtained having the following expression:

$$\chi = \frac{\frac{N\mu^2}{3k_B}}{T - \frac{2\mu^2}{9k_B} U\left(x_1^f, x_1^i, x_2^f, x_2^i\right)} \quad . \tag{11}$$

Here, the function $U(x_1^i, x_1^f, x_2^i, x_2^f)$ is defined as:

$$U(x_1^f, x_1^i, x_2^f, x_2^i) = \frac{L_1(x_1^f, x_1^i, x_2^f, x_2^i)}{(x_1^f - x_1^i)(x_2^f - x_2^i)} \tag{12}$$

where x_1^f and x_1^i are the maximum and minimum separation between the first and the second particles. x_2^f and x_2^i are the maximum and minimum separation between the first and the third particles. The function L_1 is defined as:

$$L_1 = 2\int_{x_1^i}^{x_1^f}\int_{x_2^i}^{x_2^f}\left(\frac{1}{x_1^3} + \frac{1}{x_2^3} + \frac{1}{(x_2 - x_1)^3}\right)\mathrm{d}x_1\,\mathrm{d}x_2 \quad . \tag{13}$$

By comparing Eq. 11 with the well-known Curie-Weiss law $\chi = \frac{C}{T - T_o}$, one can obtain the following expressions for the constant C and the ordering temperature T_o:

$$C = \frac{N\mu^2}{3k_B} \tag{14}$$

$$T_o = \frac{2\mu^2}{9k_B} U \quad . \tag{15}$$

T_o does not depend on the anisotropy constant. Eq. 11 suggests a ferromagnetic behavior of the system. Therefore, a ferromagnetic state will exist in this type of configuration. Moreover, a three - body interaction leads to the same behavior as for a two - body interaction. Similar magnetic behavior has been found by Odeh *et al.* [8] and Obeidat *et al.* [15] for the Dimer model.

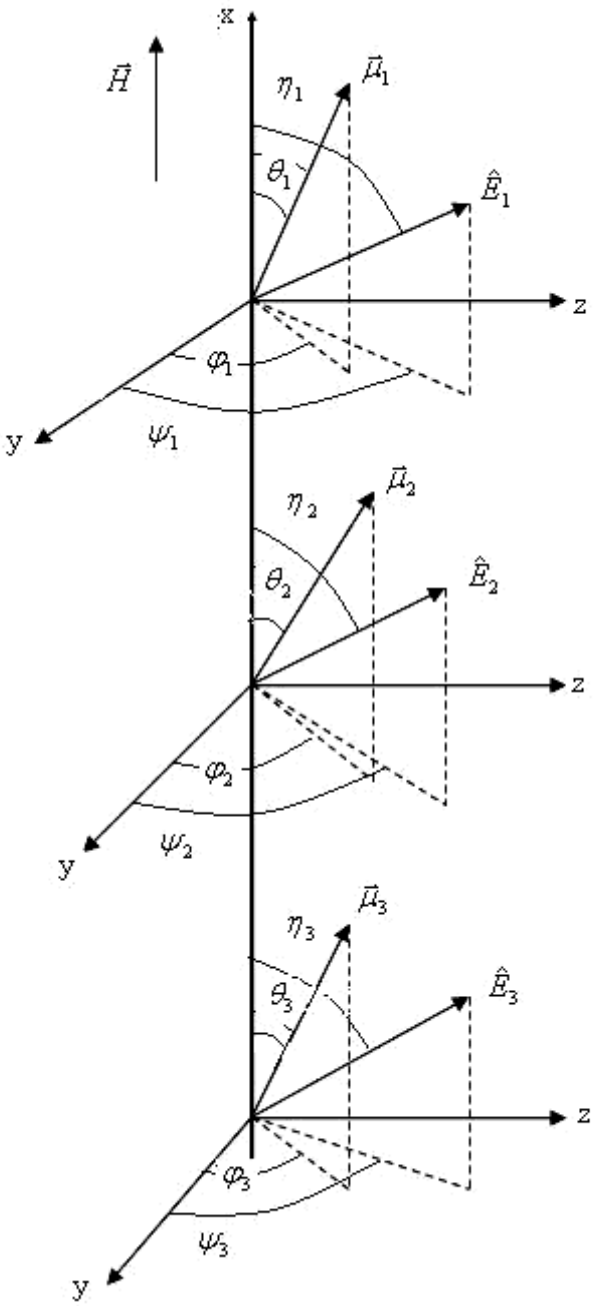

FIG. 1. Parallel configuration: Trimer model in a parallel applied magnetic field. The angles θ and φ are the polar and the azimuthal angles of the vector μ. The angles β and ψ are the polar and the azimuthal angle of the easy axis E.

Perpendicular Configuration

Fig. 2 shows the second case, where the applied magnetic field is perpendicular to the chain. In this case, the interaction energy is given by:

$$\left.\begin{aligned} E_{p-p} = & \frac{\mu^2}{y_1^2} q_1(\theta_1,\theta_2,\varphi_1,\varphi_2) \\ & + \frac{\mu^2}{y_2^2} q_2(\theta_1,\theta_3,\varphi_1,\varphi_3) \\ & + \frac{\mu^2}{(y_2-y_1)^2} q_3(\theta_2,\theta_3,\varphi_2,\varphi_3) \end{aligned}\right\} \quad (16)$$

where y_1 is the separation between the first and the second particles, while y_2 is the separation between the first and the third particles. The functions q_1, q_2 and q_3 are given by:

$$\left.\begin{aligned} q_1(\theta_1,\theta_2,\varphi_1,\varphi_2) = & \\ & 3\sin\theta_1\sin\theta_2\sin\varphi_1\sin\varphi_2 \\ & -\sin\theta_1\sin\theta_2\cos(\varphi_1-\varphi_2) \\ & -\cos\theta_1\cos\theta_2 \\ q_2(\theta_1,\theta_3,\varphi_1,\varphi_3) = & \\ & 3\sin\theta_1\sin\theta_3\sin\varphi_1\sin\varphi_3 \\ & -\sin\theta_1\sin\theta_3\cos(\varphi_1-\varphi_3) \\ & -\cos\theta_1\cos\theta_3 \\ q_3(\theta_2,\theta_3,\varphi_2,\varphi_3) = & \\ & 3\sin\theta_2\sin\theta_3\sin\varphi_2\sin\varphi_3 \\ & -\sin\theta_2\sin\theta_3\cos(\varphi_2-\varphi_3) \\ & -\cos\theta_2\cos\theta_3 . \end{aligned}\right\} \quad (17)$$

We have calculated the initial susceptibility by applying the same assumption as above ($\alpha < 1$), and we have found that:

$$\chi = \frac{\dfrac{N\mu^2}{3k_B}}{T + \dfrac{\mu^2}{9k_B}U\left(y_1^f, y_1^i, y_2^f, y_2^i\right)} . \quad (18)$$

In this form, the ordering temperature is given by:

$$T_o = -\frac{\mu^2}{9k_B}U . \quad (19)$$

Here, U is the same function as for the previous case. Eq. 18 and Eq. 19 show that the initial susceptibility and the ordering temperature do not depend on the anisotropy constant. However, in this case, the ordering temperature T_o has a negative sign and its magnitude is half that of the parallel case. The negative sign of the ordering temperature suggests an anti-ferromagnetic behavior of the system. Therefore, an antiferromagnetic state exists for such configuration. Also, our results indicate that the system has the same behaviour as for the two body interaction [8, 15].

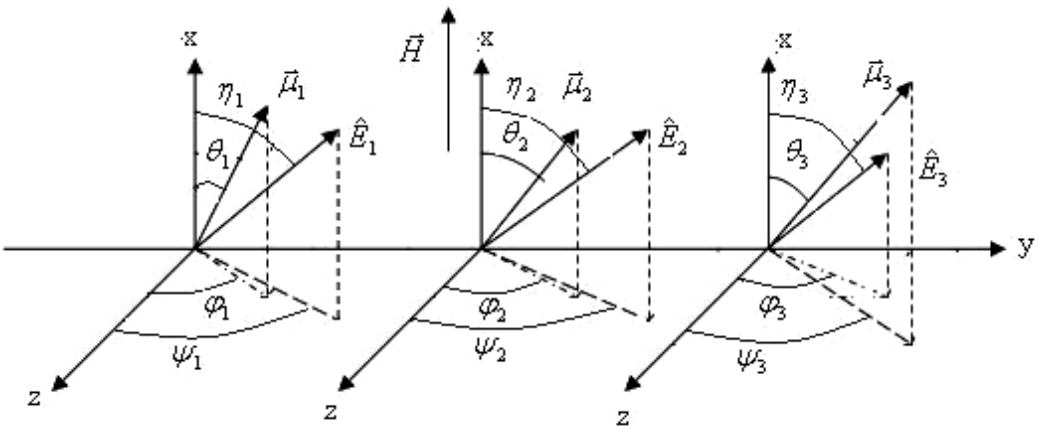

FIG. 2. Perpendicular configuration: Trimer model in a perpendicular applied magnetic field. The angles have the same meaning as in Fig. 1.

Easy Axis is Fixed Relative to the Applied Magnetic Field

As a last case, we will assume that the easy axis of the fine magnetic particles has a fixed orientation with respect to the external magnetic field. Fig. 3 shows the parallel applied magnetic field with respect to the assembly. The angle between the field and the easy axis for each particle is considered fixed at ξ. Using the same approximations as before, we have calculated the ordering temperature and found that:

$$T_o = \frac{2\mu^2}{9k_B}U + \frac{KV}{3k_B}\left(2 - 3\sin^2\xi\right) . \quad (20)$$

As can be seen form Eq. 20, the ordering temperature depends on the anisotropic constant K and the angle between the easy axis and the applied field ξ. The magnetic behavior of the system interplays between ferromagnetic and antiferromagnetic states.

Under the same condition, we have calculated the ordering temperature when the applied magnetic field is perpendicular to the chain. We found that the initial susceptibility and the ordering temperature depend on the anisotropic constant K. Our results of the ordering temperature is:

$$T_o = -\frac{\mu^2}{9k_B}U + \frac{KV}{3k_B}\left(2 - 3\sin^2\xi\right). \qquad (21)$$

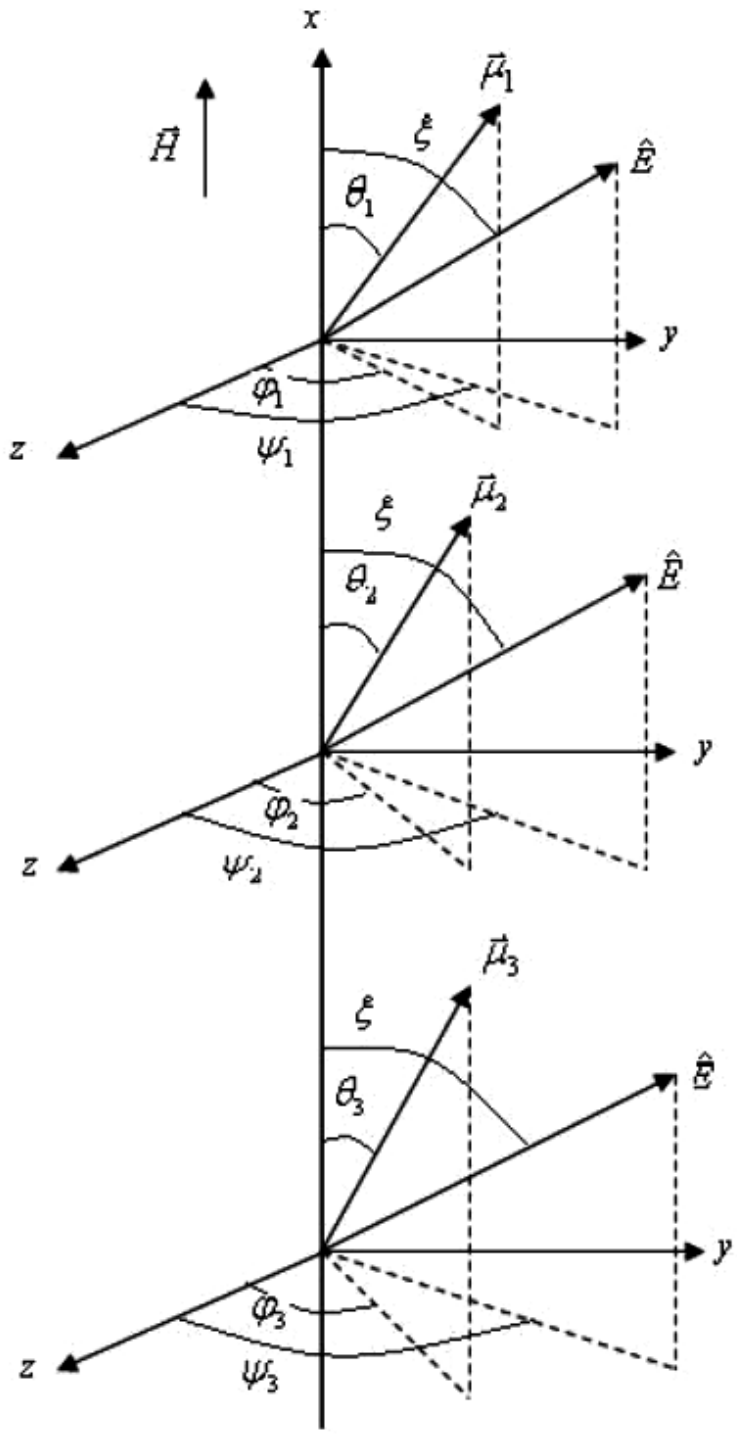

FIG. 3. Trimer model with fixed easy axis in a parallel applied magnetic field. The angles have the same meaning as in Fig. 1.

In Eq. 21, an antiferromagnetic state or a ferromagnetic state can be established depending on the parameters *U*, *K* and the angle ξ. In case of $\xi = \pi/2$, the ordering temperature is negative and an anti-ferromagnetic state is possessed by the system which reduces to case 2.

Table 1 shows the calculated results of the ordering temperature for Fe_3O_4. We have taken the average diameter to be 7.4 nm and the surfactant layer to be 2 nm. In the Table, the calculated values have been compared with the experimental values obtained by Popplewell *et al.* [3] and the calculated values for the Dimer model using expressions obtained by Obeidat *et al.* [15]. One can see that our model has much better results than those of the two - body particle interaction.

TABLE 1. The calculated values for the ordering temperature compared with the experimental values (Ref. [3]) and the calculated values from the expression obtained in Ref. [15]

Packing fraction		0.03	0.05	0.07
Ordering Temperature	Trimer model	19	32	45.4
	Dimer model Ref. [15]	11.37	13.26	15.5
	Exp. Values Ref. [3]	19	38	48

Conclusion

We have studied a statistical assembly consisting of a chain of *N* identical spherical particles each with a magnetic moment μ and a preferred easy magnetization axis. Our approach was carried out by considering three - body magnetic interactions (Trimer model). We have investigated three different cases. In cases 1 and 2, we have assumed a randomly oriented easy axis with the applied magnetic field parallel to the chain in case 1 and perpendicular to the chain in the second case. Our results for case 1 showed that a transition into ferromagnetic state can occur, where the ordering temperature was found to be positive. In case 2, we found that an antiferromagnetic state exists with negative ordering temperature. In the third case, where we assumed that the easy axis has a fixed direction relative to the applied magnetic field, our calculations showed that whether the applied magnetic field is parallel or perpendicular to the chain, there is a presence of both ferromagnetic and antiferromagnetic states depending on the anisotropy constant *K*, the particle separations through the parameter *U* and the orientation of the easy axis relative to the applied field ξ. Moreover, one can adjust the parameters ξ and *U* in a solid matrix and predict the magnetic state. The calculated ordering temperature for Fe_3O_4 shows much better values than those of the Dimer model.

Acknowledgements

This work was supported by the Jordan University of Science and Technology, grant number 205-2007.

References

[1]Menear, S., Bradbury, A. and Chantrell, R.W., J. Magn. Magn. Mater. 39 (1983) 17.

[2]Ayoub, N.Y., Kobeissi, M.A., Chantrell, R.W., O'Grady, K. and Popplewell J., J. Phys. F: Metal Phys. 15 (1985) 2229.

[3]Popplewell, J., Abu-Aisheh, B. and Ayoub, N.Y., J. Appl. Phys. 64 (1988) 5852.

[4]Ayoub, N.Y., Abu-Aisheh, B., Laham, N. and Popplewell, J., IEEE Tran. Magn. 25 (1989) 3860.

[5]Morup, S.J., IEEE Tran. Magn. 23 (1987) 5.

[6]Chantrell, R.W., Ayoub, N.Y. and Popplewell, J., J. Magn. Magn. Mater. 53 (1985) 199.

[7]Raikher, Yu. L., J. Magn. Magn. Mater. 39 (1983) 11.

[8]Odeh, I., Abdallah, A.K., Dababneh, M.S., Laham, N.M. and Ayoub, N.Y., The Arabian Journal for Science and Engineering, 19 (1994) 697.

[9]Ayoub, N.Y., Shamoun, A., Abdallah, A.K., Dababneh, M.S., Odeh, I.M. and Laham, N.M., J. Magn. Magn. Mater. 127 (1993) 75.

[10]Smirnov, S.I. and Komogortsev, S.V., J. Magn. Magn. Mater. 320 (2008) 1123.

[11]Thiaville, A., J. Magn. Magn. Mater. 182 (1998) 5.

[12]Thiaville, A., Phys. Rev. B, 61 (2000) 12221.

[13]Mamiya, H., Nakatani, I. and Furubayashi, T., Phys. Rev. Lett. 84 (2000) 6106.

[14]Gruyters, M., J. Magn. Magn. Mater. 320 (2008) 407.

[15]Obeidat, A.A., Gharaibeh, M.A., Al-Safadi, D., Al-Samarah, D.H., Qaseer, M.K.H., Ayoub, N.Y., J. Supercond. Nov. Magn. 22 (2009) 805.

Volume 3, Number 1, 2010. pp. 25-30

Jordan Journal of Physics

ARTICLE

Atomic Form Factor of Some Tissue- Equivalent Materials at 25.2keV Photon Energy Using Geant4 Toolkit

Hanan H. Saleh[a]

[a] *Department of Physics, Faculty of Science, Al- Hussein Bin Talal University, P.O. Box (20), Ma'an, Jordan.*

Received on: 15/4/2010; Accepted on: 16/6/2010

Abstract: Using Geant4 toolkit, the differential cross-section and the atomic form factor for coherent scattering of 25.2 keV photons in some tissue- equivalent compounds at 90° were calculated. The results gave good agreement with those calculated theoretically.

PACS: 87.50.-a, 87.53.-j

Keywords: Coherent scattering; Incoherent scattering; Tissue- equivalent materials; Geant4.

Introduction

At low energies, as in diagnostic radiology or nuclear medicine, coherent and incoherent scattering play an important role in the interaction of photons with matter.

Coherent and incoherent scattering are subject to some limitations, mainly self-attenuation of the primary and scattered radiations within the material and the multiple scattering of the radiation. But this doesn't limit the interest increase of using them in the public safety sector, detection of explosives in the passenger luggage and food inspection [1-3]. The unique scattering signature they gave, which is characteristic of the material, enhanced their use in the field of tissue characterization in the medical environment and in other industrial applications [4].

In diagnostic problems, using of tissue - equivalent materials is recommended to detect any change in the radiological properties of tissues, because of the similar density and elemental composition to real human tissues. Also, other studies support the close match with its scattering characteristics [5-7].

Experimentally, the intensity fluctuations of x-ray tubes limit their use as a photon source, and instead of that many measurements in this field were performed during the past (50) years using a narrow beam of γ-rays emitted by radioactive isotopes. However, these sources suffer from weak intensities and high energy backgrounds [8-11].

In this work, the coherent scattering cross-section and the atomic form factor of 25.2 keV photons from a set of low and close Z tissue - equivalent materials ($5.4<Z<7.6$) were calculated by simulation using CERN's toolkit "Geant4" as introduced by Gupta et al. [12] and compared with values obtained theoretically. The atomic form factor provides information about the inner structure of the atoms and macro - molecules which can be widely utilized in medical diagnostics and imaging.

Many measurements were conducted to obtain this scattering cross - section, but for larger energy and for other atomic number materials [13-14]. At 25.2 keV, we cannot resolve experimentally the coherent peak

Corresponding Author: Hanan H. Saleh. **Email**: hanan_saleh@ahu.edu.jo

from the incoherent one, but this can be achieved in simulation.

Theoretical Concepts

The scattering spectrum from the scattering material can be analyzed in such a way that one can obtain the coherent and the incoherent peaks separately. So, one can obtain the coherent scattering cross-section by comparing the area of the coherent peak with that of the incoherent peak in the spectrum and using the relation [12];

$$\frac{\left(d\sigma(\theta)/d\Omega\right)_{coh}}{\left(d\sigma(\theta)/d\Omega\right)_{inc}} = \frac{N(\theta)_{coh}}{N(\theta)_{inc}} \frac{f_s(\theta)}{f_p(\theta)} \frac{\in_{inc}}{\in_{coh}} \quad (1)$$

where:

$N(\theta)_{coh}$ and $N(\theta)_{inc}$ are the photo-peak area of the coherent and incoherent spectrums, respectively, at an angle θ from the scatterer.

$f_s(\theta)$ is the attenuation factor for the incoherently scattered photons.

$$\left.\begin{aligned} f_s(\theta) &= \frac{I}{I_0} = \exp[-\mu_{inc} x] \\ &= \exp[-\sigma_{inc} \rho x] \end{aligned}\right\} \quad (2)$$

$f_p(\theta)$ is the absorption factor for the coherently scattered photons.

$$\left.\begin{aligned} f_p(\theta) &= \frac{I_{abs}}{I_0} = \frac{I_0 - I}{I_0} \\ &= 1 - \exp[-\mu_{coh} x] \\ &= 1 - \exp[-\sigma_{coh} \rho x] \end{aligned}\right\} \quad (3)$$

$\in_{coh}$ and $\in_{inc}$ are the photo-peak efficiencies of the detector for the coherently and incoherently scattered photons, respectively.

The incoherent scattering cross-section is governed by Klein Nishina cross-section in the relation:

$$\left(\frac{d\sigma(\theta)}{d\Omega}\right)_{inc} = S(x,Z)\left(\frac{d\sigma(\theta)}{d\Omega}\right)_{KN} \quad (4)$$

$S(x, Z)$ is the incoherent atomic scatter function that represents the effect of the electron binding energy, Z is the effective atomic number of the scatterer and x is the photon momentum transfer (= $(\sin(\theta/2))/\lambda$), where θ is the angle of scattering and λ is the wavelength of the incident radiation. In our case, all the samples were low Z materials, so the coupling between electrons and between electrons and nuclei is small compared to the photon energies used; i.e. $S(q,Z) \approx Z$. And

$$\left.\begin{aligned} \left(\frac{d\sigma(\theta)}{d\Omega}\right)_{KN} &= \frac{r_0^2}{2} \frac{1}{[1+Y(1-\cos\theta)]^2} \times \\ &\left[1+\cos^2\theta + \frac{Y^2(1-\cos\theta)^2}{1+Y(1-\cos\theta)}\right] \end{aligned}\right\};$$

$Y = E_0 / m_0 c^2$, r_0 is the classical electron radius.

Substituting these values for Y, $\left(\frac{d\sigma(\theta)}{d\Omega}\right)_{KN}$ and $\in_{inc} / \in_{coh}$, one can simplify Eq. 1 to be:

$$\left.\begin{aligned} &\left(\frac{d\sigma(\theta)}{d\Omega}\right)_{coh} = \\ &K \times Z \frac{(\exp[-\sigma_{inc}\rho x])}{(1-\exp[-\sigma_{coh}\rho x])} \frac{N(\theta)_{coh}}{N(\theta)_{inc}} \end{aligned}\right\} \quad (5)$$

K is the system constant that depends on the geometry of the experiment, the probability of scattering of photons and on the system parameters and can be calculated from the previous relations.

With such ratio method, the effect of multiple scattering within the sample is illuminated.

$F(x, Z)$ can be calculated from the relation:

$$F(x,Z) = \left[\frac{(d\sigma(\theta)/d\Omega)_{coh}}{(d\sigma/d\Omega)_T}\right]^{1/2} \quad (6)$$

where $(d\sigma/d\Omega)_T$ is Thomson scattering cross - section.

There are three main atomic form factor theories used in the literature; the non relativistic form factor (NRFF), the relativistic form factor (RFF) and the relativistic modified form factor (RMFF)

which give different theoretical values extending over a wide momentum transfer range for many elements. There are small discrepancies between their values, but all of them show a direct increase with increasing the atomic number of the sample and an indirect relationship with momentum transfer increase, as represented in Fig. 1. Extracting the results to $1.4344A^{-1}$ gives values which can be used for comparison.

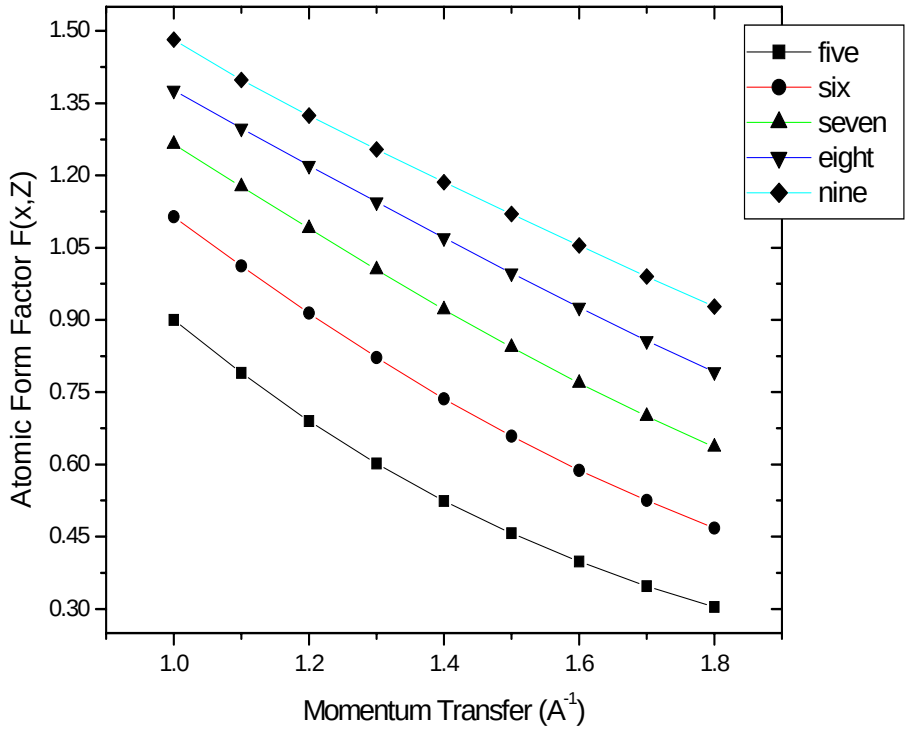

FIG. 1. The atomic form factor vs. momentum transfer for different atomic number elements as obtained from (RFF) theory [15].

Geant4 and the Modeled Experiment

Geant4 is a free Monte Carlo toolkit written in C++ for the simulation of the passage of particles in matter designed and developed at CERN by world wide collaboration [16]. It has a very rich set of physics models for a wide energy range to handle the interaction of particles with matter. Geant4 provides a diverse, wide-ranging, comprehensive toolkit that includes a powerful kernel for tracking, geometry, detector response, run, event, step management, visualization and user interfaces.

The user of Geant4 must build his own code by himself that cover [17] the geometry of the system, materials and particles involved, the generation of primary events and tracking through materials and electromagnetic fields and the governing physics processes, the response of sensitive detector components, the generation of event data and also, the analysis of simulation data at different levels of detail.

Fig. 2 provides the modeled experiment which is used in this work. The geometrical dimensions of the entire components of the detector are obtained from the manufacturer of a real one in the x-ray lab.

A beam of 25.2 keV photons is generated by the gun and passes through a narrow collimator with a rectangular slit of (4×1) mm dimension to form a pencil like beam then directed towards the sample. Another identical collimator is used in the way of the scattered beam in front of the Si(Li) detector located at a scattering angle of 90°.

Measurements were performed using some tissue - equivalent materials; Polyethylene, Cholesterol, Lucite, Water, White-matter, Muscle and Blood of cylindrical geometries of (12) mm radius and (15) mm length.

The stored energy deposition data resulting from the simulation is analyzed to generate a histogram, so one can resolve the coherent and incoherent peaks from the total histogram, as shown in Fig. 3.

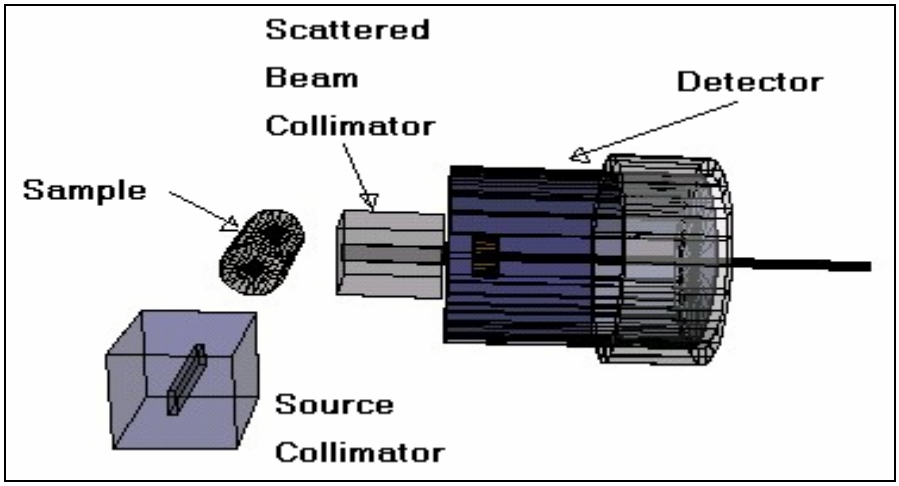

FIG. 2. Geometry of the setup as modeled in the simulation codes.

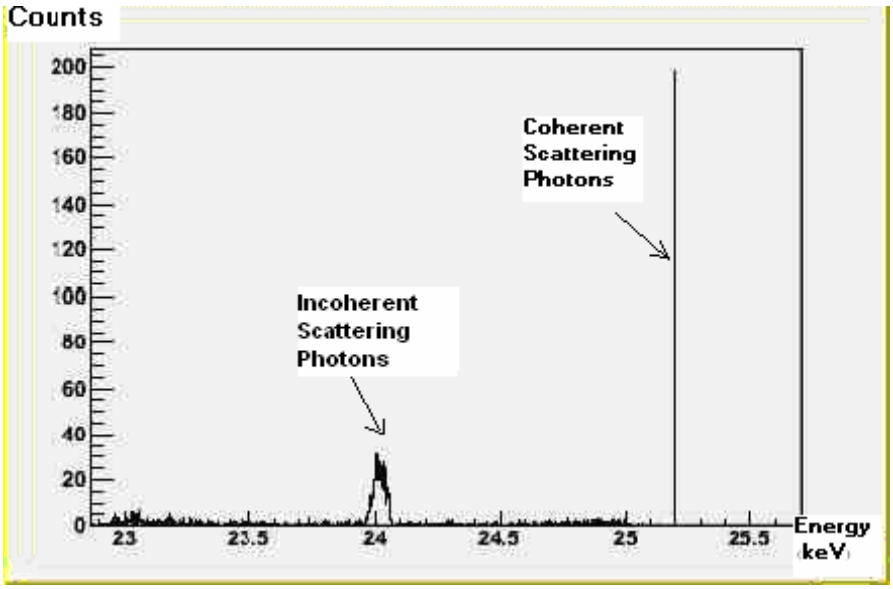

FIG. 3. The output spectrum obtained by the simulation.

Results and Discussion

The scattered spectrums were collected using an old model of Si(Li) detector. Its efficiencies at the incident and the scattered energies were obtained by simulation.

A million of photons were incident toward the detector first with the primary energy then with the scattered energy, and in every case we measured the number of photons in the full energy peak and divided it by one million. The relative efficiency $\epsilon_{inc}/\epsilon_{coh}$ is:

$$\epsilon_{inc}/\epsilon_{coh} = 1.0305 .$$

For each sample, differential coherent cross - sections and their corresponding form factors are given in Table 1 along with the atomic form factor obtained theoretically.

The results in the Table show that the differential coherent cross-section increases with increasing the atomic number of the sample. The form factors are in agreement with those obtained from previous theories. There is a better agreement with relativistic modified form factor (RMFF). Meanwhile, RFF predicts higher values.

A graphical representation of the results, shown in Fig. 4, shows the closer agreement of Geant4 results with the RMFF theory.

TABLE. 1. Differential coherent cross-sections and form factors for 25.2 keV at (90°) obtained by simulation.

Sample	$\overline{Z}$	$(\frac{d\sigma}{d\Omega})_{coh}$ (barn/atom.st)	Atomic Form Factor F*(x,Z)*			
			Geant4	RMFF[18]	RFF[15]	NRFF[19]
PE	5.4439	0.0106±0.0006	0.5173±0.0030	0.5489	0.5860	0.5794
Cholesterol	5.6483	0.0118±0.0007	0.5458±0.0030	0.5721	0.5898	0.5956
Lucite	6.4673	0.0179±0.0011	0.6723±0.0051	0.6662	0.6849	0.6612
Water	7.4167	0.0231±0.0015	0.7631±0.0068	0.7774	0.7952	0.7384
W-matter	7.4965	0.0243±0.0016	0.7819±0.0069	0.7869	0.8045	0.7449
Muscle	7.5269	0.0247±0.0016	0.7889±0.0070	0.7905	0.8080	0.7474
Blood	7.6132	0.0254±0.0017	0.7997±0.0077	0.8007	0.8181	0.7545

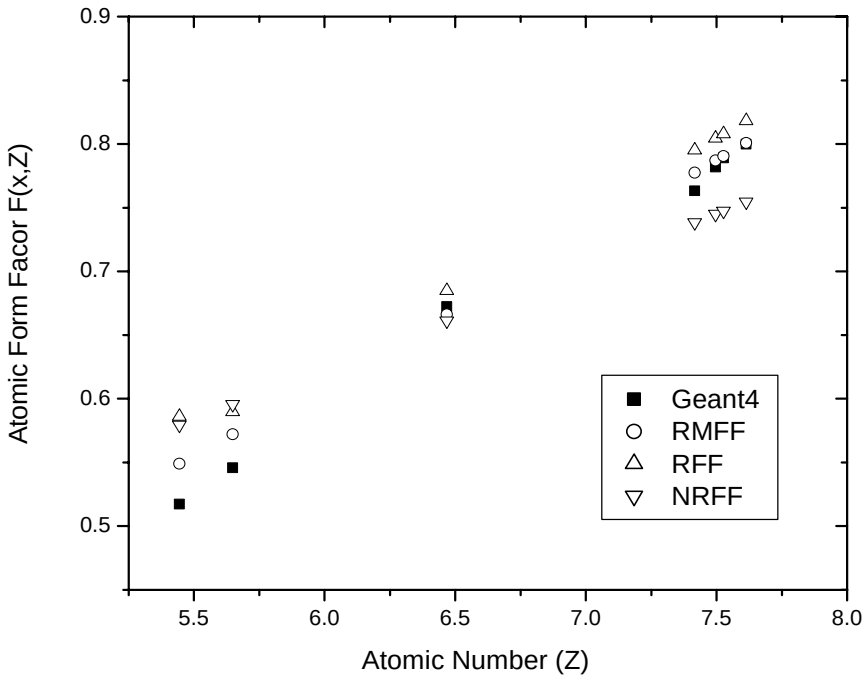

FIG. 4. Atomic form factor as a function of atomic number.

The error in the cross-sections arises from statistical errors and at most reaches a percentage of 5.8%. Increasing the number of incident primaries will decrease this error, but the cost of this process will be the increase in the simulation run-time and thus the need to more powerful computers.

As the atomic number of the sample increases, the discrepancy about the RMFF theory values decreases, since the binding energy of the electrons participating in the scattering will decrease.

The literature reviewed showed other experiments which assure the superiority of RMFF theory for intermediate ($1<x<10A^{-1}$) and high momentum transfer ($x>10A^{-1}$) [10, 14].

For heavier materials such as those used in [20], RFF gives higher values of the resulting form factor, but RMFF is still the most compliant.

Conclusions

The presented differential coherent cross-sections and the atomic form factors for some low Z tissue-equivalent materials at intermediate momentum transfer $1.4344A^{-1}$ are seen to be in good agreement with those obtained from the RMFF theory, which confirms its appropriateness in finding the coherent atomic form factor. The simulated results demonstrate the capability of using Geant4 to characterize tissue- equivalent materials of close low atomic numbers when

the sample length is 15mm, which encourages using it in further radiation and medical physics applications.

A further study on biological and industrial materials, using Geant4 toolkit at higher momentum transfer is being demonstrated.

References

[1]Harding, G. and Schreiber, B., Rad. Phys. Chem. 56(1-2) (1999) 229.

[2]McFarlane, N.J.B., Bull, C.R., Tillett, R.D., Speller, R.D., Royle, G.J. and Johnson, K.R.A., J. Agri. Eng. Res. 75(3) (2000) 265.

[3]Chatterjee, B.K., LaJohn, L.A. and Roy, S.C, Rad. Phys. Chem. 75(12) (2006) 2165.

[4]Sharaf, J.M., Appl. Radiat. Isot. 54(5) (2001) 801.

[5]Koç, N. and Özyol, H., Rad. Phys. Chem. 59(4) (2000) 339.

[6]Poletti, M.E., Gonçalves, O.D. and Mazzaro, I., Nucl. Instr. Meth. Phys. Res. B213 (2004) 595.

[7]Akar, A., Baltaş, H., Çevik, U., Korkmaz, F. and Okumuşoğlu, N.T., J. Quant. Spect. Radiat. Trans. 102(2) (2006) 203.

[8]Gupta, S.K.Sen, Paul, N.C., Bose, J., Das, S.C. and Chaudhuri, N., Nucl. Instr. Meth. Phys. Res. 193 (1982) 395.

[9]Parthasaradhi, K., Esposito, A. and Pelliccioni, M., Int. J. Rad. Appl. Instr. 43(12) (1992) 1481.

[10]İçelli, O. and Erzeneoğlu, S., Spectrochimica Acta Spect. Acta B: At. Spect. 56 (2001) 331.

[11]Kurucu, Y., J. Elec. Spect. Rel. Phen. 142(1) (2005) 39.

[12]Gupta, S.K.Sen, Paul, N.C., Roy, S.C. and Chaudhuri, N., J. Phys. B: At. Mol. Phys. 7 (1979) 1211.

[13]Elshemey, W.M., Elsayed, A.A. and El-Lakkani, A., Phys. Med. Biol. 44 (1999) 2907.

[14]Nayak, N.G. and Siddappa, K., Rad. Phys. Chem. 71(3-4) (2004) 673.

[15]Hubbell, J. H. and Overbo, I., J. Phys. Chem. Ref. Data 8 (1979) 69.

[16]Barca, G., Castrovillari, F., Chauvie, S., Cuce, D., Foppiano, F., Ghiso, G., Guatelli, S., Lamanna, E., Lopes, M.C., Peralta, L., Pia, M.G., Rodrigues, P., Trindade, A. and Veltri, M., Nucl. Phys. B125 (2003) 80.

[17]Sorel, M., MiniBooNE Tech. Note # 103 (2005). Version 2.

[18]Schaupp, D., Schumacher, M., Smend, F., Rullhusen, P. and Hubbell, J. H., J. Phys. Chem. Ref. Data 12 (1983) 467.

[19]Hubbell, J.H., Veigele, Wm.J., Briggs, E.A., Brown, R.T., Cromer, D.T. and Howerton, R.J., J. Phys. Chem. Ref. Data 4 (1975) 471.

[20]Gonçalves, O.D., De Barros, S., Eichler, Nucl. Instr. Meth. Phys. Res. A: Accel. Spect. 280(2-3) (1989) 375.

Volume 3, Number 1, 2010. pp. 31-40

Jordan Journal of Physics

ARTICLE

Effect of Electric Field on Surface and Center of Ferroelectric Film

Ahmad Musleh Alrub[a]

[a] *Physics Department, Al-Hussein Bin Talal University, Ma'an, 20, 71111, Jordan.*

Received on: 6/4/2010; Accepted on: 21/6/2010

Abstract: Size, surface and temperature effects of first and second order phase transition of ferroelectric (FE) thin films have been discussed in detail in the literature. However, the reversal of polarization by an applied electric field in FE materials is an important phenomenon to the industrial and technological applications, and it is an active research area for experimentalists as well as for theories. The Tilley-Zeks model has well described the polarization profiles of FE thin films in the absence of electric field. Hence, we adopt the Tilley-Zeks model of free energy expression and a term *P.E*, which gives the energy due to the interaction of electric field *E* and polarization *P*, included in the free energy expression. We study the effects of electric field on polarization profile for second order FE thin films with different surface parameters for the case when the direction of electric field is along the direction of polarization (induced polarization phenomenon) and the case when the electric field is in opposite direction with the polarization (polarization reversal phenomenon). We have found that the switching time decreases with increasing the value of external electric field.

PACS: 77.80.Fm.

Keywords: Polarization reversal; Tilley-Zeks model; Electric field; Switching time.

Introduction

Due to the recent development in thin-film fabrication techniques, there is an increasing number of applications of ferroelectric materials in microelectronics, such as nonvolatile memory, random access memory, microwave devices and micro-electro-mechanical systems. A number of advantages are expected from thin film based devices; for example, light weight, small volume, high density, high switching speed and low power consumption [1, 2].

Experimentally, finite size effect has long been studied since the 1960s. Various techniques including x-ray diffractometry (XRD), Raman scattering, second harmonic generation (SHG), differential scanning calorimetry (DSC), specific heat, dielectric constant and static polarization measurements have been employed [3-10].

Distinct physical properties have been observed in thin film from these experiments which are completely different from their counterparts in bulk form. Consequently, thickness dependence of various physical properties in ferroelectric films has been extensively studied [1].

Ferroelectricity is a result of collective behavior of many interacting dipoles. For a bulk sample, this interaction is so strong that the surface effect can be ignored. The size effect can be visualized as the influence due to the presence of a surface layer with completely different properties from those in the interior layers of the film[11-15] and the introduction of inhomogeneous polarization profile $(dp/dz)^2$ incorporation of the extrapolation length delta such that $dp/dz = \pm p/\delta$ [16, 17].

Corresponding Author: Ahmad M. Alrub. **Email**: AhmadAlrub@ahu.edu.jo

Landau Devonshire (LD) theory is successfully applied to bulk ferroelectrics [18, 19]. Kretschmer and Binder [20] set out a framework for finite material in which polarization (p) is treated as a function of coordinate (z) normal to the film. Tilley and Zeks [16] and Ong *et al.* [21] showed that the polarization profile *p*(*z*) within the film can be expressed in terms of Jacobi elliptic functions for the symmetric second-order films. Tan *et al*. [22, 23] numerically studied the first order transition for thin film in detail. However, a group of authors investigated the properties of the polarization reversal of ferroelectric film for second order phase transition based on Tilley-Zeks model by using step field, sinusoidal and bipolar electric field [24-27]. For completeness, in this paper we study the effect of electric field on polarization profile when the electric field is in the same and the opposite direction to the polarization.

Theory and Modeling

In this paper, we study the effect of electric field on polarization, so we consider a symmetric thin FE film of thickness L extending along the z axis, from $-L/2$ to $L/2$. The FE material is assumed to undergo a second-order phase transition. The model is one-dimensional with polarization and related physical quantities varying as a function of z. The direction of polarization may be parallel to the film surface, so the effect of the depolarization field is negligible. We can also assume an FE film with a polarization direction normal to the film surface where we can ignore the depolarization field for FE materials with finite conductivity [28] or for FE materials in short-circuited capacitors [29]. The Landau-Devonshire free energy per unit area for the thin film with thickness L under an action of an electric field E is expressed as [16, 30]:

$$\left.\begin{aligned}\frac{G}{S}=\int_{-\frac{L}{2}}^{\frac{L}{2}}&\left[\begin{aligned}&\frac{a(T-T_c)}{2\varepsilon_o}P^2+\frac{B}{4\varepsilon_o^{\,2}}P^4\\&+\frac{D}{2\varepsilon_o}\left(\frac{dP}{dz}\right)^2-EP\end{aligned}\right]dz\\&+\frac{D}{2\varepsilon_o\delta}\left(P_-^{\,2}+P_+^{\,2}\right)\end{aligned}\right\};\qquad(1)$$

where S is the cross-sectional area of the film with plane surface at $z=\pm(L/2)$ and $P_\pm=(\pm L/2)$ is the polarization value at the boundaries. Here, a and B are temperature-independent parameters. For a second-order phase-transition material, B has a positive value and T_c is the Curie temperature of the material. The coefficient D is associated with the spatial variation of P along the z direction. The factor of ε_0 in Eq. 1 is to ensure that a, B and D have simple mechanical dimensions [31] .The effect of electric field is included in -*E.P* term. The inhomogeneity of the film, where the polarization varies as a function of distance (*z*) across the film thickness, can be represented by the term $(dp/dz)^2$. The surface and size effects of the film are studied by introducing the so-called extrapolation length δ leading to the boundary conditions.

$$\frac{dP}{dz}=\pm\frac{P}{\delta}\ \text{ at }\ z=\pm\frac{L}{2}.\qquad(2)$$

For a positive δ, the polarization is depressed at the surface and for a negative value, it is enhanced [16]. For numerical presentation, it is convenient to scale all variables. We let $t=T/T_C$, $p=P/P_0$ with $P_0^{\,2}=\varepsilon_0 aT_C/B$ and $e=E/E_0$ with $E_0^{\,2}=4a^3T_C^{\,3}/27\varepsilon_0 B$. P_0 and E_0 are the equilibrium bulk polarization and the bulk coercive field at $T=0$, respectively. With this scaling, we then have the reduced free energy as:

$$\left.\begin{aligned}F=\int_{-l/2}^{l/2}&\left[\begin{aligned}&\frac{1}{2}(t-1)p^2+\frac{1}{4}p^4\\&+\frac{1}{2}\left(\frac{dp}{d\zeta}\right)^2-\frac{2}{3\sqrt{3}}ep\end{aligned}\right]d\zeta\\&+\frac{1}{2\delta_r}(p_-^{\,2}+p_+^{\,2})\end{aligned}\right\};\qquad(3)$$

where:

$F=BG/a^2T_C^{\,2}\xi_0 S$, $\zeta=a^{1/2}T_C^{\,1/2}z/D^{1/2}$, with $\xi_0^{\,2}=D/aT_C$ corresponding to the characteristic length of the material. $\delta_r=\delta/\xi_0$ and l is related to L in the same

way as ζ to z. The scaled boundary conditions now become:

$$\frac{dp}{d\zeta} = \pm\frac{p}{\delta_r} \text{ at } \zeta = \pm\frac{l}{2}. \quad (4)$$

This scaling has the advantage that all FE materials in the same class are represented by the same universal curves. For a film, the basic assumption is that the equilibrium $p(\zeta)$ corresponds to a minimum of F, so that $p(\zeta)$ is a solution of the Euler Lagrange equation:

$$\frac{d^2p}{d\zeta^2} = (t-1)p + p^3 - \frac{2}{3\sqrt{3}}ep. \quad (5)$$

We solve Eq. 5 numerically by the use of an error controlled fourth-order Runge-Kutta (RK) routine [32], and the forming of polarization profile will obey the boundary conditions in Eq. 4. The polarization reversal is studied by using the phenomenological Landau-Khalatnikov (LK) equation which can be written as [33]:

$$\left.\begin{aligned}\gamma\frac{\partial P}{\partial\tau} &= -\frac{\partial(F/S)}{\partial P}\\ &= -\frac{A(T-T_C)}{\varepsilon_0}P - \frac{B}{\varepsilon_0^2}P^3\\ &\quad + \frac{D}{\varepsilon_0}\frac{d^2P}{dz^2} + E\end{aligned}\right\} \quad (6)$$

where τ is the time. The scaled form of LK equation is:

$$\left.\begin{aligned}\frac{\partial p}{\partial\tau_r} &= -\frac{\partial f}{\partial p}\\ &= (1-t)p - p^3\\ &\quad + \frac{d^2p}{d\zeta^2} + \frac{2}{3\sqrt{3}}e\end{aligned}\right\} \quad (7)$$

where the reduced time τ_r is given by $\tau_r = \tau(AT_C\zeta_0/\varepsilon_0\gamma)$. The delay in domain movement is represented by the parameter γ, the coefficient of viscosity. The kinetic term $m(\partial^2P/\partial t^2)$ is neglected in the LK equation, because it only contributes to phenomena in the higher frequency range.

The global order parameter is the average polarization of the film which can be written as:

$$\bar{p} = \frac{1}{l}\int_{-l/2}^{l/2} p(\zeta)\, d\zeta \quad (8)$$

The free energy of the bulk is:

$$F = \frac{A(T-T_C)}{2\varepsilon_o}P^2 + \frac{B}{4\varepsilon_o^{\,2}}P^4 - EP, \quad (9)$$

and in the reduced form is:

$$f = [(t-1)/2]p^2 + (1/4)p^4 - \frac{2}{2\sqrt{3}}ep. \quad (10)$$

At equilibrium; $df/dp = 0$, $d^2f/dp^2 = 0$, the coercive field of the bulk can be derived as:

$$E_C = \frac{2}{3\sqrt{3}}\left[\frac{A^{3/2}(T_C-T)^{3/2}}{\varepsilon_0^{1/2}\beta^{1/2}}\right]. \quad (11)$$

The reduced form of coercive field is:

$$e_{cb} = \left(\sqrt{1-t}\right)^3. \quad (12)$$

Results and Discussion

Fig. 1 shows the effect of electric field *e* on polarization profile in an FE film of thickness $l = 1.5$ with positive extrapolation length $\delta_r = 4.0$. The direction of the electric field is the same as the direction of polarization. The electric field induces polarization inside the film, and it is observed that by increasing the value of *e*, the polarization increases in the film center and on the film surface. In Fig. 1, we can see that the effect of *e* on the polarization at film center is different from the effect of *e* on the polarization on the film surface, so we manifest the difference in Fig. 2 for a wide range of *e* values. Fig. 2 shows that the polarization increment at the film center is slightly larger than the polarization increment on film surface and this increment increases with increasing the value of *e*.

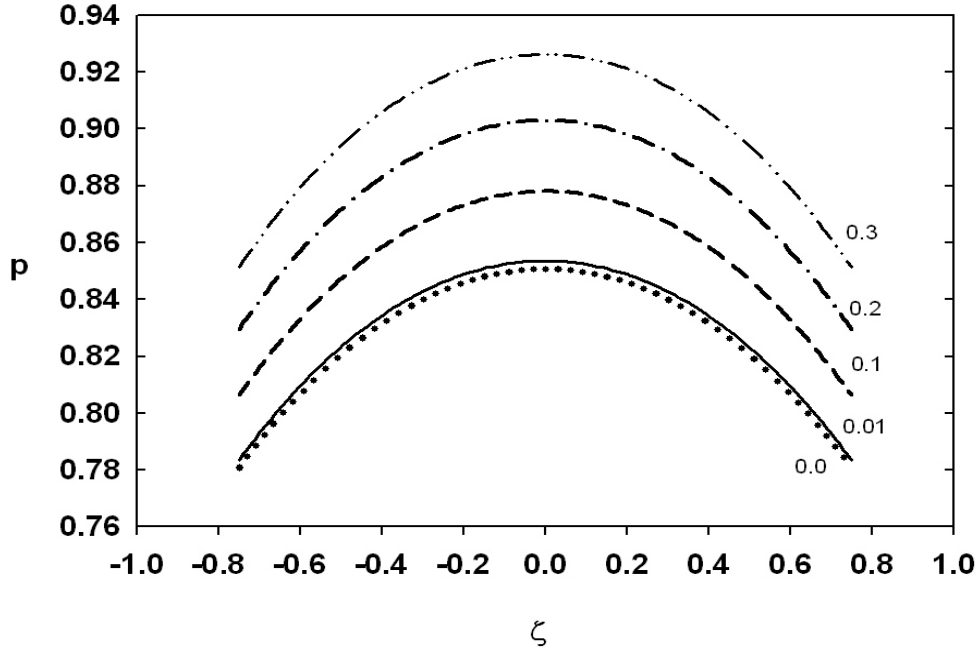

FIG. 1. Polarization *p* versus ζ for electric field *e* equal to 0.0, 0.01, 0.1, 0.2 and 0.3. Thickness *l* = 1.5, extrapolation length $\delta_r = 4.0$, temperature *t* = 0.0.

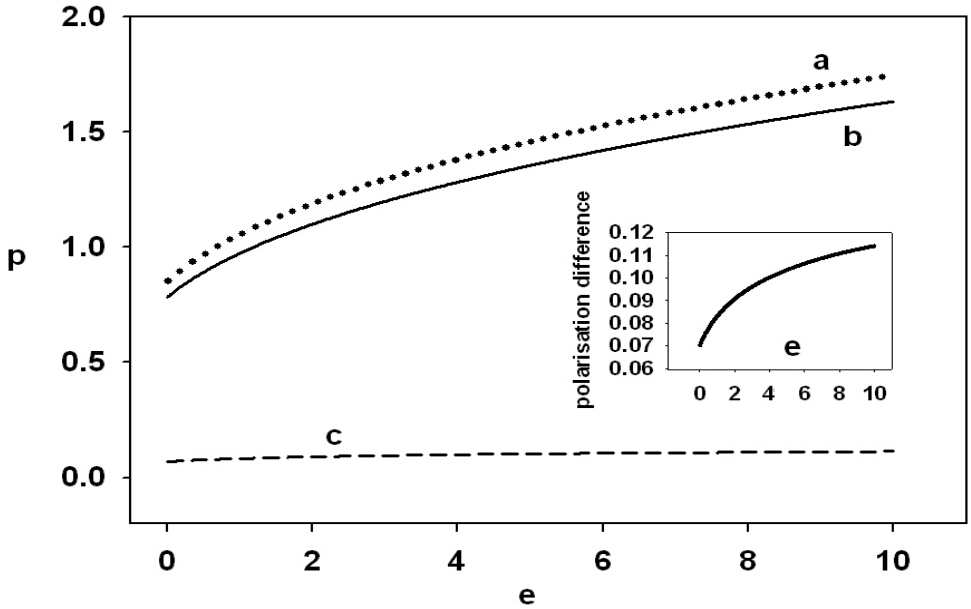

FIG. 2. Polarization *p* versus electric field *e*. Curve (a) corresponds to electric field effects at the film center , curve (b) corresponds to the electric field effects on the film surface, curve (c) represents the difference between curves (a) and (b). Film thickness *l* = 1.5, extrapolation length $\delta_r = 4.0$, temperature *t* = 0.0. Curve (c) zoom in inset.

Fig. 3 shows the electric field *e* effect on polarization of an FE film with a thickness $l = 1.5$ with negative extrapolation length $\delta_r = -4.0$. The electric field direction is the same as the direction of polarization. Hence *e* induces polarization inside the film, so by increasing *e* the polarization increases. The figure shows that there is a difference in increment of induced polarization between the film center and the film surface which can also be visualized in Fig. 4. In the contrary to a film with positive extrapolation length (Fig. 2), the polarization increment on the film surface is slightly greater than the polarization increment at the film center for films with negative extrapolation lengths.

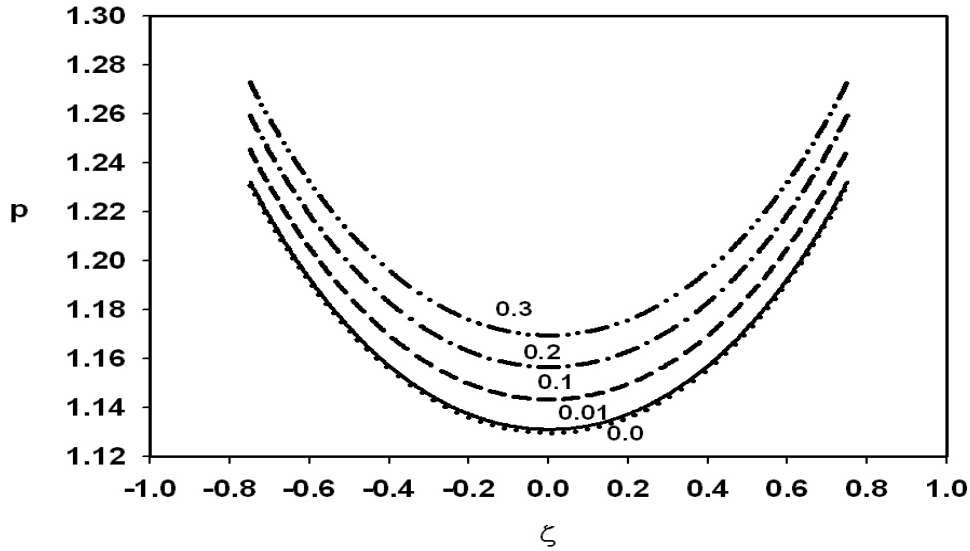

FIG. 3. Polarization *p* versus ζ for electric field *e* equal to 0.0, 0.01, 0.1, 0.2 and 0.3. Thickness *l* = 1.5, extrapolation length $\delta_r = -4.0$, temperature *t* = 0.0.

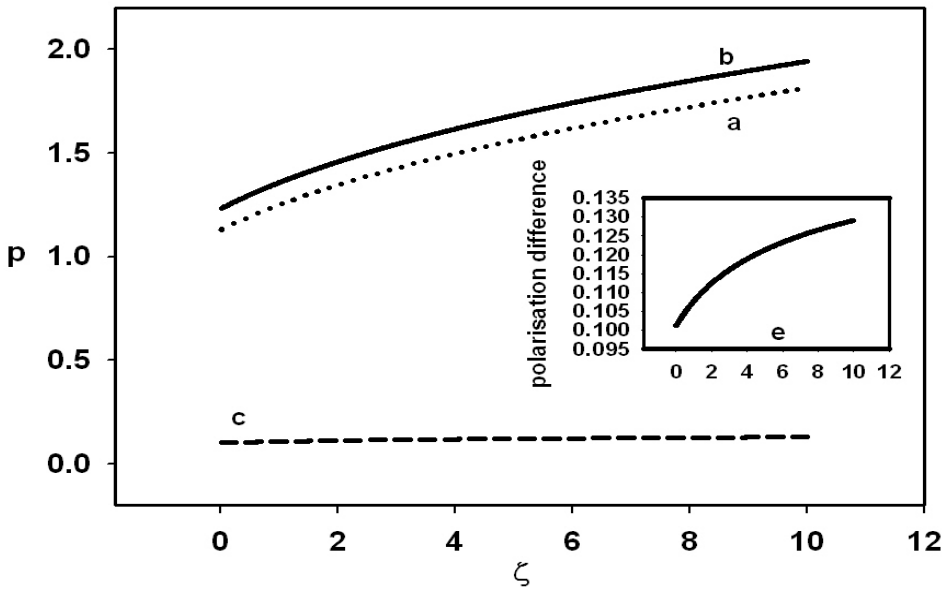

FIG. 4. Polarization *p* versus electric field *e*. Curve (a) corresponds to electric field effects at the film center, curve (b) corresponds to the electric field effects on the film surface, curve (c) represents the difference between curves (b) and (a). Film thickness *l* = 1.5, extrapolation length $\delta_r = -4.0$, temperature *t* = 0.0. Curve (c) zoom in inset.

The polarization reversal of FE films is studied by applying the step electric field that is usually used in experiments [34]. The most significant quantity in polarization reversal is the switching time τ_S. There are several definitions of switching time in the literature [18, 35-41]. In this study, we adopt the switching time τ_S to be the time taken when the switching current *J* drops to 90% of its maximum value $J_{\max}$ [38-40]. The initial polarization in the film is switched from its negative value in all the simulations. The form of the step field is:

$$e = e_0 \theta(\tau_r) \tag{13}$$

where $\theta(\tau_r)$ is a step function defined as:

$$\theta(\tau) = \begin{cases} 1 & \text{for } 0 \le \tau_r < \tau_0 \\ 0 & \text{for } \tau_0 \end{cases} \tag{14}$$

where τ_0 is the time when the field is switched off and e_0 is the amplitude of the electric field. By applying the step electric field, we present the effects of electric field on the switching of ferroelectric films.

The study on domain formation and its movement in ferroelectricity is one of the important and complicated problems in switching phenomena. Under a certain applied field at any time during switching, the polarization profile can be simulated from Eq. 7. This polarization profile during switching for an FE film with $\delta_r = +2$ and a film thickness l = 5.4 is analyzed from the graphs in Fig. 5 and Fig. 6 by applying electric fields $e = 0.9e_c$ and $e = 5e_c$, respectively at t = 0.0 for both films. e_c is the coercive field of the bulk given in Eq. 12. A close look at Fig. 5 and Fig. 6 shows that the dipole moments on the surface are switched before the dipole moments in the film interior. This is because the polarization on the film surface is less than that at the film centre for an FE film with $+\delta_r$ (see Fig. 1). Hence, the polarization on the film surface would switch before that at the film center. Experimentally, it is well known that polarization switches first on the film surface then in the bulk [42]. Fig. 5 and Fig. 6 show that by increasing the applied electric field e, the switching time τ_S decreases for a film of thickness $l = 5.4$ at $t = 0.0$. It can be seen in Fig. 6 that the initial polarization of an FE film with $+\delta_r$ can be completely reversed by the applied electric field $e = 0.9\ e_c$. This value of e is less than the bulk coercive field e_c. The reason for that the film is switched by the electric field less than the value of e_c can be explained based on the curves in Fig. 1 for $p(\zeta)$ of a film with positive δ_r. The polarization is suppressed on the surface compared with the value at the center, and even at the center, polarization is lower than that of the bulk case, $p = 1$ for bulk at $t = 0$ and at $e = 0$ (Eq. 10). In this respect, the value of average polarization (Eq. 8) of this film is less than the value of bulk polarization. Hence, we may deduce that switching would take place more readily in the film with $+\delta_r$ than in the bulk at lower applied field ($e < e_c$).

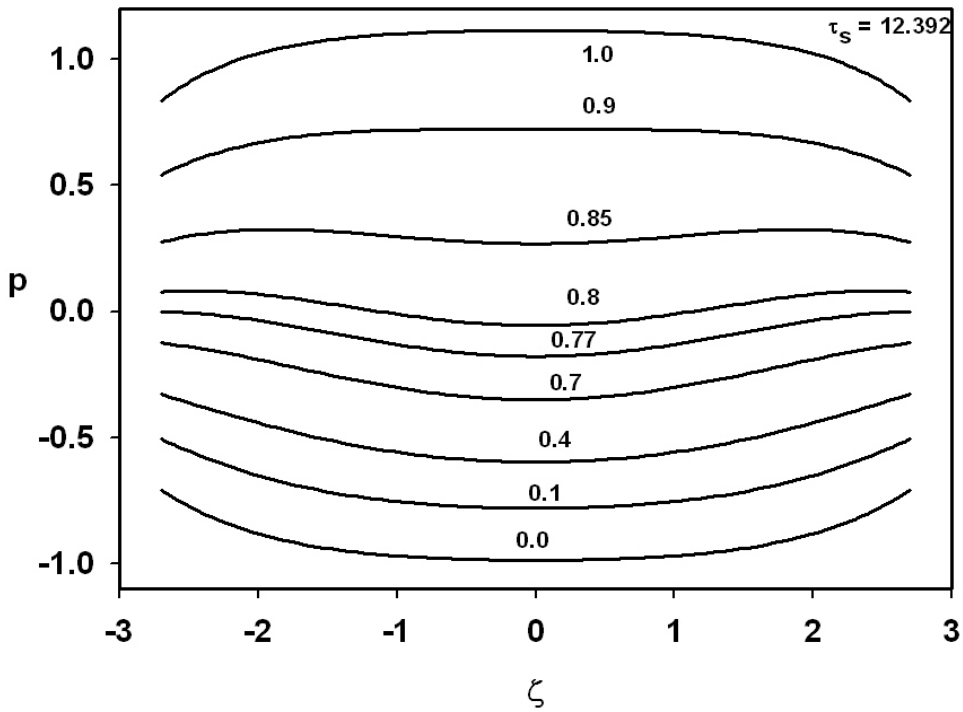

FIG. 5. Polarization profile $p(\zeta)$ during switching for thin film. l = 5.4, δ = +2, $e = 0.9e_c$, t = 0.0. The number at each curve represents the time taken to reach the stage in terms of fraction of $\tau_S = 12.392$.

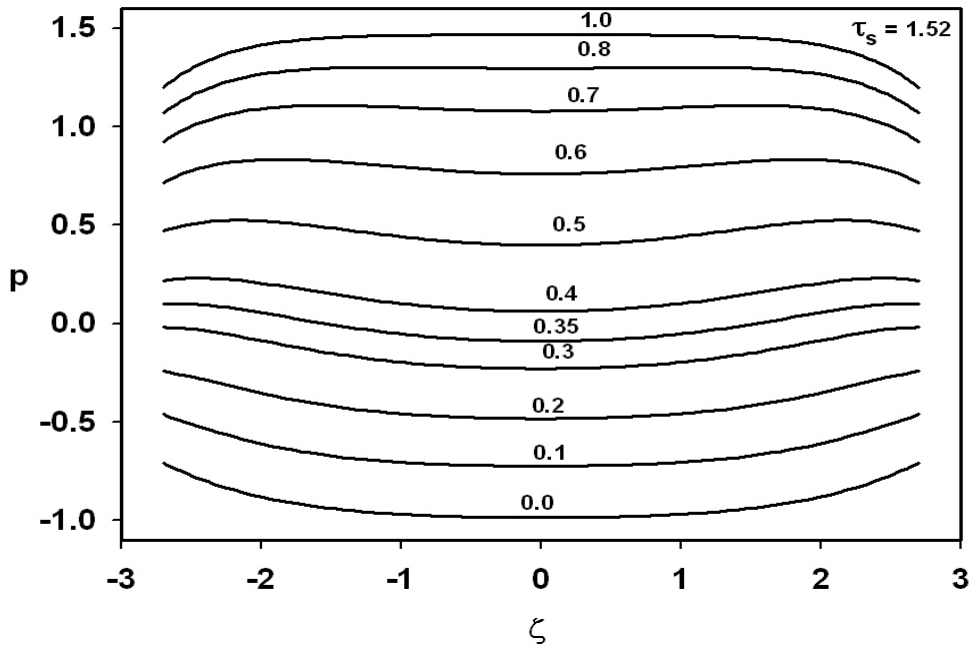

FIG. 6. Polarization profile $p(\zeta)$ during switching for thin film. l = 5.4, δ_r = +2, e = 5e_c, t = 0.0. The number at each curve represents the time taken to reach the stage in terms of fraction of $\tau_S = 1.52$.

Fig. 7 and Fig. 8 show the polarization profile during switching for an FE film with a negative extrapolation length $\delta_r = -2$ for film thickness $l = 5.4$ at temperature $t = 0$. It is obvious that switching of dipole moments at the film center takes place before that on the film surface. This phenomenon is contrary to what we observed in the FE film with $+\delta$ (Fig. 5 and Fig. 6); that is switching happens on the surface before at the film center. For an FE film with $-\delta_r$, the polarization on the surface is greater than that at the center due to the surface effect with negative extrapolation length (See Fig. 3).

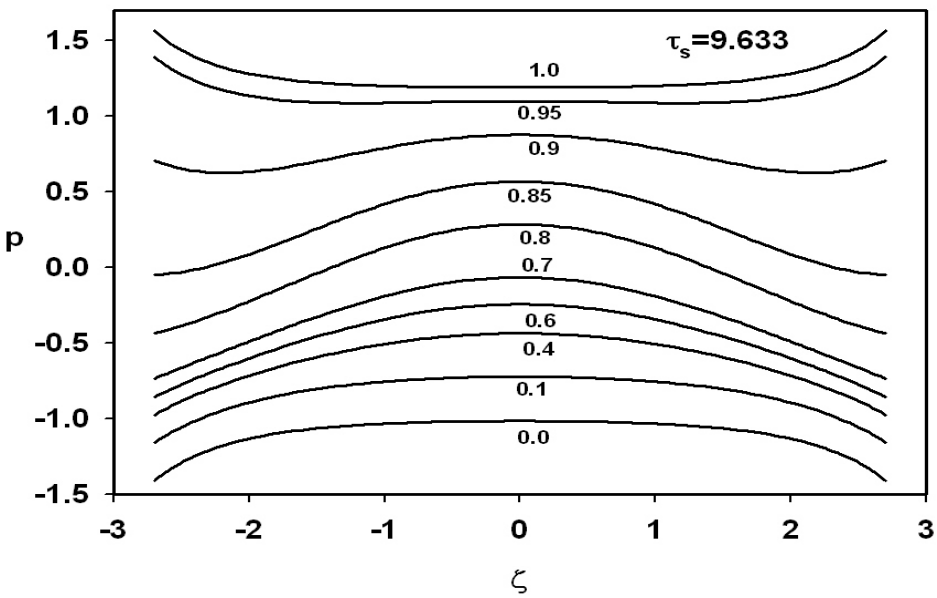

FIG. 7. Polarization profile $p(\zeta)$ during switching for film thickness l = 5.4, $\delta_r = -2$, e = 1.5, t = 0.0. (Film parameters are the same as those of a film with $+\delta_r$, see Fig. 5). Polarization profile stages are taken from bottom to top at 0.0, 0.1, 0.4, 0.6, 0.7, 0.8, 0.85, 0.9, 0.95 and 1.0 in terms of fraction of $\tau_S = 9.633$.

Fig. 7 and Fig. 8 indicate that the switching time τ_S of an FE film with a negative extrapolation length decreases with increasing the value of the applied external electric field. This result is the same as that for an FE film with positive extrapolation length. The switching time ($\tau_S = 1.52$) of an FE film with $l = 5.4$ and $\delta_r = +2$ is less than the switching time ($\tau_S = 1.661$) of an FE film with $l = 5.4$ and $\delta_r = -2$ at $t = 0$ by applying the same value of electric field $e = 5e_c$ as shown in Fig. 6 and Fig. 8, respectively. The author in Ref. [25] shows that for an FE film with a positive extrapolation length, the switching time and coercive field decrease with decreasing film thickness, and these characteristics may be useful for memory devices.

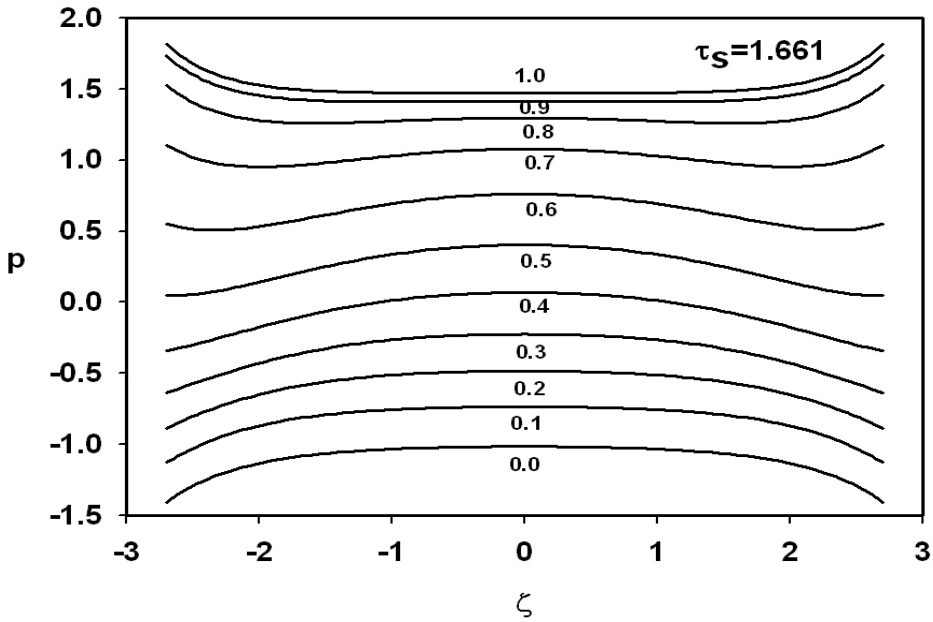

FIG. 8. Polarization profile $p(\zeta)$ during switching for film thickness l = 5.4, $\delta_r = -2$, e = 5ec, t = 0.0. (Film parameters are the same as those of a film with + δ_r , see Fig. 5). Polarization profile stages are taken from bottom to top at 0.0, 0.1, 0.2, 0.3 0.4, 0.5, 0.6, 0.7, 0.8, 0.9 and 1.0 in terms of fraction of $\tau_S = 1.661$.

Conclusion

Landau-typed TZ model is used to study the intrinsic switching phenomenon of a free standing FE film. We study the effects of electric field on polarization in FE films on the surface and at the center of the film. Two directions of applied electric field with respect to the polarization direction are taken into account. It is found that switching time decreases with increasing the value of the applied field for FE films with positive and negative extrapolation lengths. Polarization switching takes place on the film surface before that at the film center for an FE film with a positive extrapolation length, while for an FE film with a negative extrapolation length the matter is reversed. When the direction of the applied field is in the direction of polarization, we found that the increment of induced polarization of an FE film due to applied field on film surface is different from that at the film center for both FE films with different signs of extrapolation length.

Acknowledgements

I sincerely thank Dr. Ong Lye Hock for his useful comments.

References

[1]Dawber, M., Rabe, K.M. and Scott, J.F., Rev. Mod. Phys. 77 (2005) 1083.

[2]Scott, J.F., J. Phy.: Condenced Matter, 18 (2006) 361.

[3]Glass, A.M., Phys. Rev. 172(2) (1968) 564.

[4]Zhdanov, V.G., Kostov, E.G., Malinovisky, V.K., Pokrovsky, L.D. and Srerelyuknina, L.N., Ferroelectrics, 29 (1981) 219.

[5]Hochli, U.T. and Rohrer, H., Phys. Rev. Lett. 48(3) (1982) 188.

[6]Scott, J.F., Duiker, H.D., Beale, P.D., Pouligny, B., Dimmler, K., Parris, Butler, M. and Athems, D. S., Physica B+C, 150 (1988) 160.

[7]Liu, W.G., Kong, L.B., Zhang, L.Y. and Yao, X., Solid State Comm. 93(8) (1995) 653.

[8]Ducharme, S., Fridkin, V.M., Bune, A.V., Palto, S.P., Blinov, L.M., Petukhova, N.N. and Yudin, S.G., Phys. Rev. Lett. 84(1) (2000) 175.

[9]Tybell, T., Ahn, C.H. and Triscone, J.-M., App. Phy. Lett. 75(6) (1999) 856.

[10]Kushida, K. and Takeuchi, H., Ferroelectrics, 108 (1990) 3.

[11]Larsen, P.K., Dormans, G.J.M., Taylor, D.J. and Van Veldhoven, P.J., J. Appl. Phys. 76(4) (1994) 2405.

[12]Miller, S.L., Nasby, R.D., Schwank, J.R., Rodgers, M.S. and Dressendorfer, P.V., J. of App. Phys. 68(12) (1990) 6463.

[13]Tagantsev, A.K., Landivar, M., Colla, E. and Setter, N., J. Appl. Phys. 78(4) (1995) 2623.

[14]Kay, H.F. and Dunn, J.W., Philos. Mag. 7 (1962) 2027.

[15]Tagantsev, A.K., Integr. Ferroelectr. 16 (1997) 237.

[16]Tilley, D.R. and Zeks, B., Solid State Commun. 49 (1984) 823.

[17]Cottam, M.G., Tilley D.R. and Zeks, B., Solid State Commun. 17 (1984) 1973.

[18]Fatuzzo, E. and Merz, W.J., "Ferroelectricity", North-Holland Pub. Co.; Wiley, Interscience (Publishers Division, Amsterdam, New York, 1967).

[19]Lines, M.E. and Glass, A.M., "Principles and applications of ferroelectrics and related materials", (Clarendon Press, Oxford [Eng.], 1977).

[20]Kretschmer, R. and Binder, K., Phys. Rev. B, 20(3) (1979) 1065.

[21]Ong, L.H., Osman, J. and Tilley, D.R., Phys. Rev. B, 63(14) (2001) 144109.

[22]Tan, E.K., Osman, J. and Tilley, D.R., Solid State Commun. 116 (2000) 61.

[23]Tan, E.K., Osman, J. and Tilley, D.R., Solid State Commun.117 (2001) 59.

[24]Musleh, A. and Ong, L.H., AIP Conference Proceedings 1150/1 (2009) 274.

[25]Musleh, A.M., Ong, L.-H. and Tilley, D.R., J. App. Phys. 105(6) (2009) 061602.

[26]Ong, L.H. and Musleh, A., Ferroelectrics, 380 (2009) 150.

[27]Ong, L.H., Musleh, A.,Osman, J., Journal Fizik Malaysia, 29/1&2 (2008) 11.

[28]Watanabe, Y., Phys. Rev. B, 57(2) (1998) 789.

[29]Kittel, C., "Introduction to Solid State Physics". (John Wiley & Sons, Inc., New York, Chichester, Brisbane, Toronto, Singapore, 1996).

[30]Binder, K., Ferroelectrics, 35 (1981) 99.

[31]Osman, J., Ishibashi, Y. and Tilley, D.R., Jpn. J. Appl. Phys. 37 (1998) 4887.

[32]Press, W.H., Flannery, B.P., Teulosky S.A. and Vetterling, W.T., "Numerical Recipes in Fortran 77: The Art of Scientific Computing". (Cambridge University Press, Cambridge, 1997).

[33]Blinc, R. and Zeks, B., "Soft Mode in Ferroelectrics and Antiferroelectrics". (North-Holland Publishing Company, Amsterdam, 1974).

[34]Merz, W.J., J. Appl. Phys. 27(8) (1956) 938.

[35]Ishibashi, Y., Jpn. J. Appl. Phys. 31 (1992) 2822.

[36]Ishibashi, Y., J. Phys. Soc. Jpn. 59(11) (1990) 4148.

[37]Nagaya, T. and Ishibashi, Y., J. Phys. Soc. Jpn. 60(12) (1991) 4331.

[38]Cummins, S.E., J. Appl. Phys. 36(6) (1965) 1958.

[39]Omura, M., Adachi, H. and Ishibashi, Y., Jpn. J. App. Phys. 31 (1992) 3238.

[40]Katayama, T., Shimizu, M. and Shiosaki, T., Jpn. J. Appl. Phys. 32(9A) (1993) 3943.

[41]Shibashi, Y. and Orihara, H., J. Phys. Soc. Jpn. 61(12) (1992b) 4650.

[42]Merz, W.J., Phys. Rev. 95(3) (1954) 690.

المراجع

[1]Swinbank, A.M., Bower, R.G., Smith, G.P., Wilman, R.J., Smail, I., Ellis, R.S., Morris, S.L. and Kneib, J.P., MNRAS, 376 (2007) 479.

[2]Trott, C. and Webster, R., International Astronomical Union Symposium no. 220, held 21-25 July 2003, Sydney, Eds. Ryder S. D. *et al*. (2003) p. 109.

[3]Schneider, P., "Gravitational lensing as a probe of structure", in: Dark Matter and Dark Energy in the Universe, Proceedings of the XIV Canary Islands Winter School of Astrophysics, Tenerife, Spain (2003).

[4]Courbin, F., Gravitational lensing: a unique tool for cosmology, ASP Conference Series,Vol. xxx, (2003).

[5]McInnes, R.N., Institute for Astronomy, Royal Observatory of Edinburgh, Blackford Hill, Edinburgh, EH9 3HJ, Pedagogical Seminar, 25*th* March (2008).

[6]Zacek, V., (2008), "Dark matter", in: “Fundamental Interactions”, edited by Astburty, A., Khanna, F. and Moore, R., World Scientific, Proc. of the 22nd Lake Louise Winter Institute, February 2007.

[7]Heavens, A., Lect. Notes Phys. 665 (2009) 585.

[8]Rzepecki, J.P., Ph.D. Thesis, University of Heidelberg, (Germany, 2007).

[9]Branch, D., Vaughan, T. and Kantowski, R., APJ, 447 (1995) 35.

[10]Fort, B. and Mellier, Y., Gravitational lensing and test of the cosmological constant, in: Fourth Paris Cosmology Colloquium: Phrase Transition in Cosmology Euro Conference by H. de Vega and N. Sanchez (1998) p. 288.

[11]Jackson, N., Living Rev. Rel. 10 (2007) 4.

[12]Mukherjee, K., Ph.D. Thesis, University of Pittsburgh, (2005).

[13]Blandford, R.D. and Narayan, R., Annu. Rev. Astron. Astrophys. 30 (1992) 311.

[14]Narayan, R. and Bartelmann, M., in: Formation of Structure in the Universe; edited by A. Dekel and J.P. Ostriker; (Cambridge University Press, 1999) p. 360.

[15]Wambsganss, J., "Gravitational Lensing in Astronomy", Living Reviews in Relativity, (1998).

[16]Chwolson, O., APJ, 57 (1924) 238.

[17]Einstein, A., Science, 84 (2188) (1936) 506.

[18]Refsdal, S. and Surdej, J., Rep. Prog. Phys. 57 (1994) 117.

التي يوضح رسمها الشكل **(2)**. ويتضح من الشكل أن شدة تأثير بعد العدسة تتضاءل عندما تبعد العدسة كثيراً عن الراصد، وأن اتجاه تغاير الشدة يكون معاكساً لاتجاه تغاير بعد العدسة، وهو ما تشير إليه الإشارة السالبة في المعادلة (14).

ولمعرفة شدة تأثير الكثافة السطحية Σ في بعد الصورة $\alpha(\theta)$، نأخذ مشتقة بعد الصورة بالنسبة إليها بثبوت (θ) في المعادلة (9) لنحصل على:

$$\frac{\partial\alpha(\theta)}{\partial\Sigma}=\frac{\theta}{\Sigma_{crit}} \qquad (15)$$

التي نلاحظ منها أن تأثير الكثافة السطحية في بعد الصورة يكون ثابتاً.

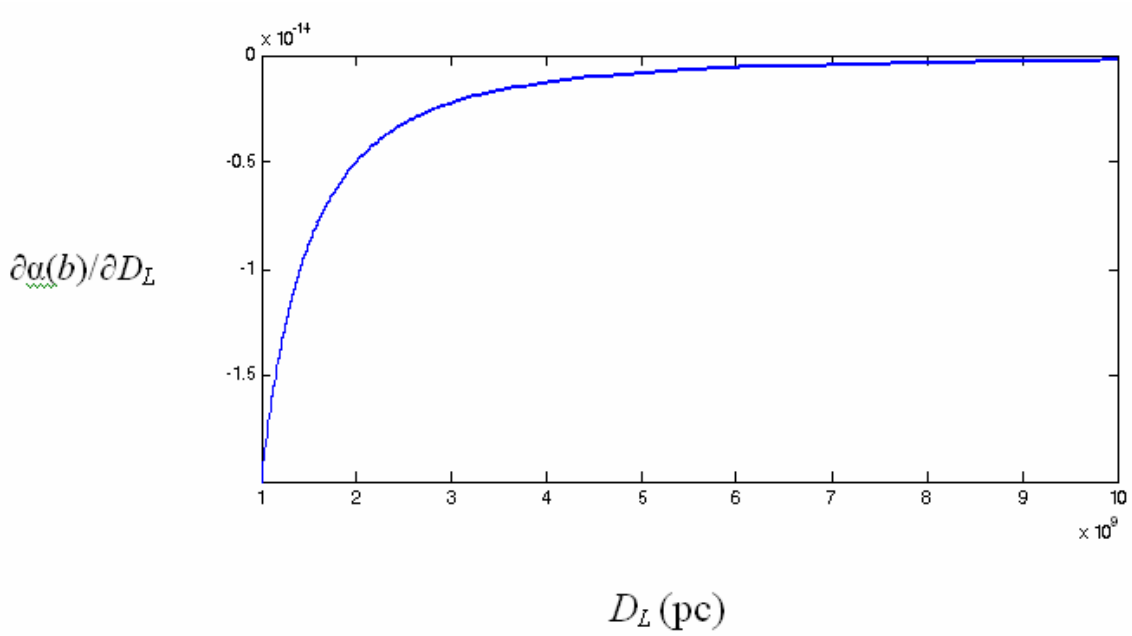

الشكل (2): شدة تأثير بعد العدسة (D_L) في تغاير بعد الصورة عن المصدر$\acute{\alpha}(\theta)$ بالنسبة إليه.

اعتمدنا في الرسم $(\frac{\Sigma}{\Sigma_{crit}}=4)$، و$(b=5\times10^3\text{pc})$ [Refsdal & Surdej, 1994][18].

الاستنتاجات العامة

إن تأثيرات الأبعاد الهندسية في موقع الصورة تختلف باختلاف النموذج التقريبي الذي يتم اعتماده. وقد يكون هذا من أسباب تباين قيمة ثابت هبل التي يتم إيجادها بواسطة عدسات الجاذبية، وذلك لأن حساب ثابت هبل باستخدام العدسات الجاذبية يعتمد على حساب زمن التأخير(time delay) الذي يعتمد بدوره على علاقة الأبعاد الهندسية مع موقع الصورة.

إن المعادلة (11) التي تعطي الزاوية المحصورة بين المحور البصري والموقع الحقيقي للمصدر تعطي المعلومات نفسها التي تعطيها معادلة العدسات المعروفة -المعادلة (3)-.

ويمكن للمعادلة (11) أن تعطينا توزيع الكتلة للمجرات أو لعناقيدها التي تتصرف كعدسة من خلال معرفة الأبعاد الهندسية للعدسة وموقع صورة مصدر معلوم، وذلك بتعويض مقدار الكثافة الحرجة وموقع الصورة والموقع الحقيقي للمصدر.

إن العلاقة بين بعد الصورة والكثافة السطحية للعدسة علاقة خطية تشير إلى أن تمايز الصورة عن المصدر يكون أوضح إذا كانت الكثافة السطحية للعدسة كبيرة، وينطبق هذا أيضاً على عرض الحزمة.

التي يمكن أن نعدها صيغة أخرى لمعادلة العدسة بدلالة كثافة الكتلة السطحية التي تحتوي ضمنياً على الأبعاد الهندسية، التي بافتراض ثبوتها تكون العوامل المؤثرة في العدسة هي كثافة الكتلة السطحية للعدسة (Σ) والكثافة الحرجة.

إن أول ما يلاحظ في المعادلة (9) أنه إذا كانت الكثافة السطحية مساوية للكثافة الحرجة فإن:

$$\alpha(\theta) = \theta \qquad (10)$$

التي تشير إلى الحصول على صورة واحدة يكون بعدها عن المصدر مساوياً لبعدها عن المحور البصري، وهي حالة مماثلة لظهور حلقة آينشتاين في عدسة الكتلة النقطية التي تكون الصورة فيها بشكل حلقة محيطة بالعدسة، والتي تظهر عندما يقع المصدر على المحور البصري ($\beta = 0$). ومن السهل ملاحظة أن الافتراض ($\beta = 0$) الذي أدى إلى استنتاج ظهور الصورة على شكل حلقة[17,16] هو في الحقيقة نتيجة مباشرة للمعادلة (8) إذا ما تم تعويضها في المعادلة (3). ومن ثم يمكن أن تمثل θ في المعادلة (10) نصف قطر آينشتاين الزاوي (θ_E). وإذا ما استخدمنا المعادلة (9) في معادلة العدسات (3) فسنحصل على صيغة جديدة لمعادلة العدسة:

$$\beta = \theta\left(1 - \frac{\Sigma}{\Sigma_{crt}}\right) \qquad (11)$$

التي توضح أنه عند ($\Sigma_{crit} >> \Sigma$) تكون ($\beta = 0$)؛ بمعنى ظهور صورة المصدر على المصدر نفسه، فلا يرى الراصد صورة للمصدر. وهذا ما ينطبق مع شرط تعدد الصور ($\Sigma > \Sigma_{crit}$) المعروف. كما يتضح منها أنه عند ($\Sigma_{crit} = \Sigma$) تكون ($\beta = 0$)، وهذا يؤيد ما ذهبنا إليه من أن المعادلة (10) تمثل نصف قطر آينشتاين الزاوي (θ_E) في حال اعتماد تقريب العدسة الرقيقة. وعليه، فبإجراء تعويضات جبرية بسيطة في شرط ظهور الحلقة ($\Sigma_{crit} = \Sigma$) نحصل على نصف قطر آينشتاين الزاوي:

$$\theta_E = \left(\frac{M(b)}{\pi D_L^2 \Sigma_{crt}}\right)^{\frac{1}{2}} \qquad (12\text{-a})$$

أو:

$$\theta_E = \theta\left(\frac{\Sigma}{\Sigma_{crt}}\right)^{\frac{1}{2}} \qquad (12\text{-b})$$

الذي يمكّننا من إعادة صياغة معادلة العدسات (9) بدلالة (θ_E) لنحصل منها على المعادلة المعروفة:

$$\beta = \theta - \frac{\theta_E^2}{\theta}$$

وهي كما يلاحظ معادلة غير خطية، تشير إلى أن للمصدر الذي في الموقع (β) صورتيْن تحدد موقعهما العلاقة:

$$\theta_{\pm} = \frac{1}{2}\left(\beta \pm \sqrt{\beta^2 + 4\theta_E^2}\right) .$$

لدراسة تأثير الأبعاد الهندسية في موقع الصور، نعوض ($\theta = \frac{b}{D_L}$) في المعادلة (9) لنحصل على:

$$\hat{\alpha}(\theta) = \frac{\Sigma}{\Sigma_{crit}} \frac{b}{D_L} \qquad (13)$$

وهي علاقة تشير إلى السلوك الخطي للعلاقة بين بعد الصورة عن المصدر ($\acute{\alpha}(\theta)$) وعرض الحزمة (b) وبين والكثافة السطحية (Σ). كما تشير إلى السلوك العكسي لبعد الصورة عن المصدر مع بعد العدسة عن الراصد، أي أنه كلما ابتعدت العدسة عن الراصد اقتربت الصورة من المصدر. ويتضح من العلاقة أيضاً الفرق في تصرف عرض الحزمة (b) الذي صار خطياً (طردياً) في هذه الحالة، بينما هو عكسي في التقريب النقطي[18].

وذلك كما نرى لأن لعرض الحزمة تأثيرًا تربيعيًا طرديًا في الكتلة المولدة للمجال في حالة العدسة الرقيقة، وليس له مثل هذا التأثير في العدسة النقطية.

وللإجابة عن سؤال محتمل هو "هل يبقى تأثير بعد العدسة في موقع الصورة فاعلاً وبالشدة نفسها عند كل الأبعاد الممكنة للعدسة عن الراصد؟" نأخذ تغاير ($\acute{\alpha}(\theta)$) بالنسبة إلى (D_L) في المعادلة (13) بثبوت كل من الكثافة الكتلية السطحية للعدسة (Σ) وعرض الحزمة، لنحصل على:

$$\frac{\partial \alpha(\theta)}{\partial D_L} = -\frac{\Sigma}{\Sigma_{crit}} \frac{b}{D_L^2} \qquad (14)$$

المرصودة بعيدة جداً والمسافات الزاوية (β,θ) صغيرة جداً لا تتعدى بضع ثوانٍ قوسية[12]، وزاوية الانحناء صغيرة جداً، فإنه يتم استخدام العلاقة $\theta\, D_S = \beta\, D_S + \hat{\alpha}(b)\, D_{Ls}$، والمعادلة (2) للحصول على معادلة العدسات المعروفة:

$$\vec{\beta} = \vec{\theta} - \vec{\alpha}\left(\vec{\theta}\right) \qquad (3)$$

التي تربط بين الموقع الزاوي للصورة والموقع الزاوي للمصدر وزاوية الانحناء المخفضة. ويستثنى من هذا التقريب حالات كون العدسة ثقباً أسود أو نجماً نيوترونياً، لأن زاوية الانحناء لا تكون صغيرة في هذه الحالات ومن ثم لا يمكن استخدام تقريب $(\sin\theta = \theta)$ الذي يستخدم في الحصول على المعادلة (3).

تقريب العدسة الرقيقة ذات الكثافة السطحية المتجانسة

تقوم الدراسات النظرية لعدسات الجاذبية على نمذجتها وفق تقريبات، أهمها تقريب عدسة الكتلة النقطية الذي يفترض أن كتلة العدسة مركزة في نقطة، وتقريب العدسة الرقيقة الذي يفترض أن كتلة العدسة منتشرة على شكل صفيحة، باعتبار أنه عندما تكون العدسة مجرة أو عنقودًا من المجرات، فإن مقارنة المسافة الفاصلة بين المصدر والراصد التي هي حوالي (1Gpc) مع قطر المجرة الموازي لخط الرؤية –سمكها– الذي هو (50 kpc) في حالة المجرة أو (1000 kpc) في حالة عنقود من المجرات، تتيح اعتبار هذا السمك صفراً، ومن ثم اعتبار العدسة صفيحة كتلوية رقيقة. وفي هذه الحالة تسمى العدسة ،العدسة الرقيقة (thin lens). وتسمى منطقة الانحناء مستوى العدسة. ويمثل الخط العمودي على مستويي العدسة والمصدر المحور البصري للعدسة. وتمثل نقطة تقاطعه مع مستوى العدسة مركز العدسة.

يتيح هذا التقريب التعامل مع الأشعة التي تمر من أية نقطة من مستوى العدسة كما هو الحال مع عدسة شفافة. فتكون زاوية انحناء الأشعة بفعل المجال الجاذبي دالة في بعد موقع مرور الأشعة عن مركز العدسة –عرض الحزمة– (b) وفي الكثافة الكتلية السطحية للعدسة (Σ). فتكون الكتلة المسببة للانحناء:

$$M(b) = 2\pi \int_0^b \Sigma(b')\, b'\, db' \qquad (4)$$

حيث $M(b)$ هي كتلة دائرة نصف قطرها (b). وتكون زاوية الانحناء المتجهة:

$$\vec{\hat{\alpha}}\left(\vec{b}\right) = \frac{4G}{c^2} \int \frac{\left(\vec{b} - \vec{b}'\right) \Sigma\left(\vec{b}'\right)}{\left|\vec{b} - \vec{b}'\right|^2} d^2 b' \qquad (5)$$

حيث $\left(\vec{b} - b'\right)$ هي المسافة من نقطة الانحناء إلى مركز العدسة.

وفي حالة الكتلة المتجانسة والمتناظرة تؤخذ نقطة الأصل عند مركز العدسة فتكون الكتلة المولدة للانحناء $(M(b) = \Sigma\pi\, b^2)$، وزاوية الانحناء:

$$\alpha(b) = \frac{4G}{c^2} \Sigma \pi b \qquad (6)$$

ولأنها متناظرة، فإنه بالإمكان اختيار مستوى واحد يضم المصدر، وعرض الحزمة، والمحور البصري. وباستخدام تعريف القطر الزاوي $(\theta = \frac{b}{D_L})$، وتعويض المعادلة (2) في المعادلة (6)، نحصل على زاوية الانحناء المخفضة:

$$\alpha(\theta) = \frac{4\pi G \Sigma}{c^2} \frac{D_L D_{LS}}{D_S} \theta \qquad (7)$$

فإذا استخدم تعريف المسافة الفعالة للعدسة D: $(D = \frac{D_L D_{Ls}}{D_S})$، وكون $(4\pi G/c^2)$ مقداراً ثابتاً، فسيتم الحصول على ثابت خاص بكل عدسة هو $(4\pi GD/c^2)$، الذي يمثل مقلوبه ما يعرف بالكثافة الحرجة للعدسة[15,14,13]:

$$\Sigma_{crit} = \frac{c^2}{4\pi\, G} (D)^{-1} \qquad (8)$$

وتأخذ المعادلة (7) الصيغة:

$$\hat{\alpha}(\theta) = \frac{\Sigma}{\Sigma_{crit}} \theta \qquad (9)$$

واستخدمت التشوهات الطفيفة التي يحدثها التأثير الجاذبي للمجرات البعيدة في مسارات الأشعة في رسم خرائط أكبر المجرات والعناقيد المجرية الموجودة في الكون[5]. واستخدمت عدسات الجاذبية في التقصي عن كمية المادة المظلمة وطبيعتها[6]، وعن الطاقة المظلمة[7] في الكون. كما استخدمت في الحصول على معلومات عن المعاملات الكونية مثل الكثافة الكونية (Ω) والتاريخ الديناميكي للعناقيد المجرية[8] ومعامل التعجيل الكوني (q_0)[9] ووجود الثابت الكوني (Λ)[10] وحساب مقدار ثابت هبل (H_0)[11].

معادلة العدسات

تتكون منظومة عدسة الجاذبية - كما يوضح الشكل (1) - من مصدر بعيد مضيء يرسل الأشعة، وعدسة - هي أي جسم ذي كتلة مولدة لمجال جاذبي قادر على إحداث انحناء قابل للرصد في مسار الأشعة-، والراصد. و يمثل الخط الواصل بين الراصد والعدسة، المحور البصري للعدسة. وتمثل الزاوية المتجهة المحصورة بين المحور البصري والموقع الحقيقي للمصدر ($\vec{\beta}$) البعد الزاوي للمصدر عن المحور البصري، والزاوية المتجهة بين المحور البصري وموقع الصورة ($\vec{\theta}$) البعد الزاوي للصورة. وتكون D_L، D_{LS}، D_S هي مسافات القطر الزاوي بين الراصد والعدسة، والعدسة والمصدر، والراصد والمصدر، على التوالي. أما $\alpha(\theta)$ فهي زاوية الانحناء المخفضة (reduced deflection angle) التي تمثل البعد الزاوي بين المصدر وصورته.

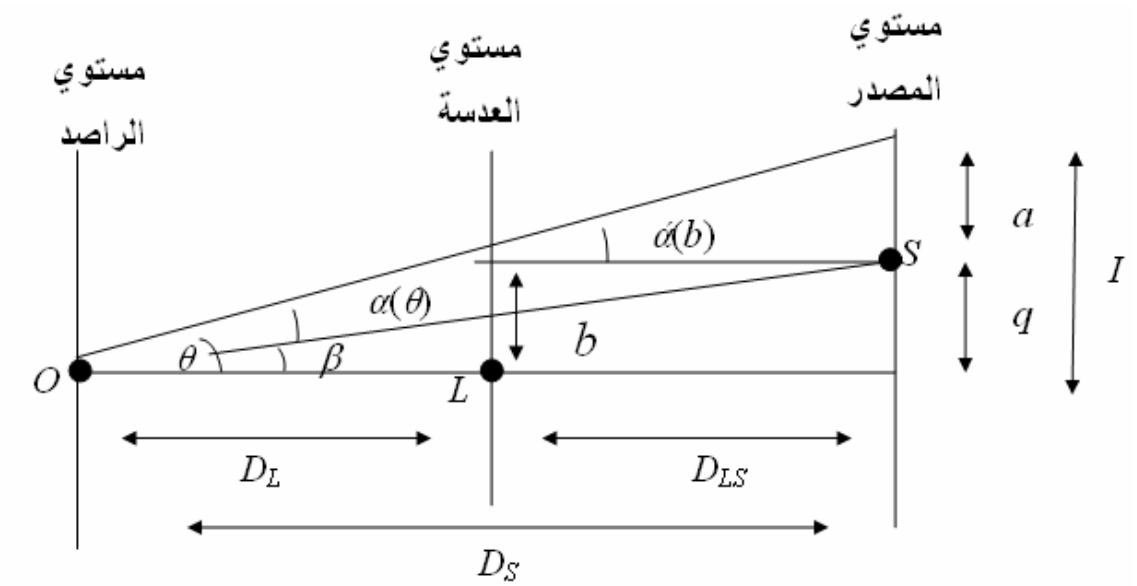

الشكل (1): شكل يوضح عدسة الجاذبية.

S المصدر الضوئي (source)؛ L العدسة (Lens)؛ O الراصد (Observer)؛ I بعد الصورة عن المحور البصري؛ q بعد المصدر عن المحور البصري؛ a بعد الصورة عن المصدر؛ β الموقع الزاوي للمصدر؛ θ الموقع الزاوي للصورة؛ $\hat{\alpha}(b)$ زاوية الانحناء (deflection angle) ؛ $\alpha(\theta)$ زاوية الانحناء المخفضة (reduced deflection angle)؛ D_L مسافة القطر الزاوي (angular diameter distance) بين الراصد والعدسة.

بحسب نظرية النسبية العامة يعاني شعاع الضوء القادم من المصدر (S) قبل أن يصل إلى الراصد (O) انحناء في مساره عند العدسة (L) بزاوية مقدارها $\hat{\alpha}(b)$، حيث

$$\hat{\alpha}(b) = \frac{4GM}{c^2 b} \qquad (1)$$

وترتبط بزاوية الانحناء المخفضة بالعلاقة:

$$\vec{\alpha}(\theta) = \frac{D_{Ls}}{D_s}\vec{\hat{\alpha}}(b) \qquad (2)$$

حيث (M) كتلة العدسة، و(G) ثابت الجاذبية، و(c) سرعة الضوء و(b) عرض الحزمة. ونظرًا لأن المصادر

المجلد 3، العدد 1، 2010. ص ص. 41-46

المجلة الأردنية للفيزياء

ARTICLE

تأثير الأبعاد الهندسية في موقع الصور الناتجة عن عدسة جاذبية رقيقة

M. A. Al-Obayde[a] and **S. A. Abrahem**[a]

[a] *Physics Department, College of Science, Mosul University, Mosul, Iraq.*

Received on: 15/10/2009; Accepted on: 6/4/2010

الملخص: باستخدام تقريب عدسة الجاذبية الرقيقة، درس البحث تأثير الأبعاد الهندسية للعدسة - التي يكون فيها الانحناء ناتجاً عن مجرة أو عنقود مجرات - في بعد الصور عن المصدر. فتم الحصول على صيغة جديدة لمعادلة العدسات تبين العلاقة بين المتغيرات الأساسية للعدسة، وتساعد في دراسة توزيع الكتلة في المجرة أو مجموعة المجرات التي تتصرف كعدسة. وبينت النتائج أن لنموذج العدسة تأثيرًا في قيمة ثابت هبل الذي يمكن إيجاده باستخدام عدسات الجاذبية. وأوضح البحث أن تأثير بعد العدسة عن الراصد في موقع الصورة يتناقص عندما تكون العدسة بعيدة جداً عن الراصد وأن تأثير عرض الحزمة في موقع الصورة في تقريب العدسة الرقيقة يكون بعكس تأثيره الذي يظهر في تقريب عدسة الكتلة النقطية.

كلمات مفتاحية: عدسة جاذبية؛ عدسة جاذبية رقيقة؛ انحناء الضوء؛ النسبية العامة.

The Effect of Geometrical Dimensions on the Image Position of the Thin Gravitational Lens

Abstract: When the gravitational lens is a galaxy or a galactic cluster, the effect of geometrical dimensions of the lens on the separation between the source and the image has been studied by using the thin lens approximation. A new form of the lens equation has been found. This equation shows the relationships between the basic parameters of the lens and helps in studying the mass distribution in the galaxy or the galactic cluster that behaves as a lens.

This research clarifies that, at a very large distance between the observer and the lens, the effect of distance from the observer to the lens on the image position decreases. Also, it shows that the effect of the impact parameter in the thin lens approximation is opposite to that which appears in the point mass approximation.

Keywords: Gravitational lens; Thin gravitational lens; Light bending; General relativity.

مقدمة

بعد اكتشاف أول عدسة جاذبية في عام 1979 تزايد اهتمام الفلكيين وعلماء الكون بظاهرة الإحناء الجاذبي (gravitational lensing) وعدسات الجاذبية، وصارت الأخيرة أداة رئيسية للدراسات الكونية المعاصرة، ولاكتشاف أسرار الكون البعيد وخفاياه، لأنها تتصرف كتلسكوبات طبيعية تمكّن من رؤية الأجسام البعيدة التي لا يمكن رؤيتها حتى باستخدام أكبر التلسكوبات الصناعية المتطورة وأضخمها[1].

واهتمت تطبيقات الإحناء الجاذبي بدراسة الأجسام التي تكون مسؤولة عن انحناء الضوء[2]، ودراسة انتشار الكتلة على مختلف المقاييس[3]، ودراسة الصور وتشوهاتها، وتكبير المصادر الأصلية وتصغيرها[4].

Corresponding Author: M. A. Al-Obayde. **Email**: malobayde@yahoo.com

Authors Index

Subject Index

المناقشة: يجب أن تكون موجزة وتركز على تفسير النتائج.

الاستنتاج: يجب أن يكون وصفا موجزا لأهم ما توصلت إليه الدراسة ولا يزيد عن صفحة مطبوعة واحدة.

الشكر والعرفان: الشكر والإشارة إلى مصدر المنح والدعم المالي يكتبان في فقرة واحدة تسبق المراجع مباشرة.

المراجع: يجب طباعة المراجع بأسطر مزدوجة ومرقمة حسب تسلسلها في النص. وتكتب المراجع في النص بين قوسين مربعين. ويتم اعتماد اختصارات الدوريات حسب نظام Wordlist of Scientific Reviewers.

الجداول: تعطى الجداول أرقاما متسلسلة يشار إليها في النص. ويجب طباعة كل جدول على صفحة منفصلة مع عنوان فوق الجدول. أما الحواشي التفسيرية، التي يشار إليها بحرف فوقي، فتكتب أسفل الجدول.

الرسوم التوضيحية: يتم ترقيم الأشكال والرسومات والرسومات البيانية (المخططات) والصور، بصورة متسلسلة كما وردت في النص.

تقبل الرسوم التوضيحية المستخرجة من الحاسوب والصور الرقمية ذات النوعية الجيدة بالأبيض والأسود، على ان تكون أصيلة وليست نسخة عنها، وكل منها على ورقة منفصلة ومعرفة برقمها بالمقابل. ويجب تزويد المجلة بالرسومات بحجمها الأصلي بحيث لا تحتاج إلى معالجة لاحقة، وألا تقل الحروف عن الحجم 8 من نوع Times New Roman، وألا تقل سماكة الخطوط عن 0.5 وبكثافة متجانسة. ويجب إزالة جميع الألوان من الرسومات ما عدا تلك التي ستنشر ملونة. وفي حالة إرسال الرسومات بصورة رقمية، يجب أن تتوافق مع متطلبات الحد الأدنى من التمايز (1200 dpi Resolution) لرسومات الأبيض والأسود الخطية، و 600 dpi للرسومات باللون الرمادي، و300 dpi للرسومات الملونة. ويجب تخزين جميع ملفات الرسومات على شكل (jpg)، وأن ترسل الرسوم التوضيحية بالحجم الفعلي الذي سيظهر في المجلة. وسواء أرسل المخطوط بالبريد أو عن طريق الشبكة (Online)، يجب أرسال نسخة ورقية أصلية ذات نوعية جيدة للرسومات التوضيحية.

مواد إضافية: تشجع المجلة الباحثين على إرفاق جميع المواد الإضافية التي يمكن أن تسهل عملية التحكيم. وتشمل المواد الإضافية أي اشتقاقات رياضية مفصلة لا تظهر في المخطوط.

المخطوط المنقح (المعدَل) والأقراص المدمجة: بعد قبول البحث للنشر وإجراء جميع التعديلات المطلوبة، فعلى الباحثين تقديم نسخة أصلية ونسخة أخرى مطابقة للأصلية مطبوعة بأسطر مزدوجة، وكذلك تقديم نسخة إلكترونية تحتوي على المخطوط كاملا مكتوبا على Microsoft Word for Windows 2000 أو ما هو استجد منه. ويجب إرفاق الأشكال الأصلية مع المخطوط النهائي المعدل حتى لو تم تقديم الأشكال إلكترونيا. وتخزن جميع ملفات الرسومات على شكل (jpg)، وتقدم جميع الرسومات التوضيحية بالحجم الحقيقي الذي ستظهر به في المجلة. ويجب إرفاق قائمة ببرامج الحاسوب التي استعملت في كتابة النص، وأسماء الملفات على قرص مدمج، حيث يعلَم القرص بالاسم الأخير للباحث، وبالرقم المرجعي للمخطوط للمراسلة، وعنوان المقالة، والتاريخ. ويحفظ في مغلف واقٍ.

الفهرسة: تقوم المجلة الأردنية للفيزياء بالإجراءات اللازمة لفهرستها وتلخيصها في جميع الخدمات الدولية المعنية.

حقوق الطبع

يُشَكِّل تقديم مخطوط البحث للمجلة اعترافاً صريحاً من الباحثين بأنّ مخطوط البحث لم يُنْشَر ولم يُقَدَّم للنشر لدى أي جِهَة أخرى كانت وبأي صيغة ورقية أو إلكترونية أو غيرها. ويُشترط على الباحثين ملء أنموذج يَنُصُّ على نقْل حقوق الطبع لتُصبح ملكاً لجامعة اليرموك قبل الموافقة على نشر المخطوط. ويقوم رئيس التحرير بتزويد الباحثين بإنموذج نقل حقوق الطبع مع النسخة المُرْسَلَة للتنقيح. كما ويُمنع إعادة إنتاج أيٍّ جزء من الأعمال المنشورة في المجلّة من دون إذن خَطِّيٍّ مُسْبَق من رئيس التحرير.

إخلاء المسؤولية

إن ما ورد في هذه المجلة يعبر عن آراء المؤلفين، ولا يعكس بالضرورة آراء هيئة التحرير أو الجامعة أو سياسة اللجنة العليا للبحث العلمي أو وزارة التعليم العالي والبحث العلمي. ولا يتحمل ناشر المجلة أي تبعات مادية أو معنوية أو مسؤوليات عن استعمال المعلومات المنشورة في المجلة أو سوء استعمالها.

معلومات عامة

المجلة الأردنية للفيزياء هي مجلة بحوث علميّة عالمية مُحكمة تصدر عن اللجنة العليا للبحث العلمي، وزارة التعليم العالي والبحث العلمي، عمان، الأردن. وتقوم بنشر المجلة عمادة البحث العلمي والدراسات العليا في جامعة اليرموك، إربد، الأردن. وتنشر البحوث العلمية الأصيلة، إضافة إلى المراسلات القصيرة Short Communications، والملاحظات الفنية Technical Notes، والمقالات الخاصّة Feature Articles، ومقالات المراجعة Review Articles، في مجالات الفيزياء النظرية والتجريبية، باللغتين العربية والإنجليزية.

تقديم مخطوط البحث

تُرسَل نسخة أصلية وثلاث نسخ من المخطوط، مُرْفَقَةً برسالة تغطية من جانب الباحث المسؤول عن المراسلات، إلى رئيس التحرير:

أ.د. ابراهيم أبو الجرايش،
رئيس التحرير، المجلة الأردنية للفيزياء،
عمادة البحث العلمي والدراسات العليا،
جامعة اليرموك، إربد، الأردن.
هاتف : 111 11 72 2 962 00 / فرعي: 3735
فاكس : 121 11 72 2 962 00
بريد إلكتروني : jjp@yu.edu.jo

تقديم المخطوطات إلكترونيًا: اتبع التعليمات في موقع المجلة على الشبكة العنكبوتية.

ويجري تحكيمُ البحوثِ الأصيلة والمراسلات القصيرة والملاحظات الفنية من جانب مُحكِّمين اثنين في الأقل من ذوي الاختصاص والخبرة. وتُشَجِّع المجلة الباحثين على اقتراح أسماء المحكمين. أما نشر المقالات الخاصّة في المجالات الفيزيائية النَشِطَة، فيتم بدعوة من هيئة التحرير، ويُشار إليها كذلك عند النشر. ويُطْلَب من كاتب المقال الخاص تقديم تقرير واضح يتّسم بالدقة والإيجاز عن مجال البحث تمهيداً للمقال. وتنشر المجلةُ أيضاً مقالات المراجعة في الحقول الفيزيائية النشطة سريعة التغيُّر، وتُشَجِّع كاتبي مقالات المراجعة أو مُستَكتبيها على إرسال مقترحٍ من صفحتين إلى رئيس التحرير. ويُرْفَق مع البحث المكتوب باللغة العربية ملخص (Abstract) وكلمات دالة (Keywords) باللغة الإنجليزية.

ترتيب مخطوط البحث

يجب أن تتم طباعة مخطوط البحث ببنط 12 نوعه Times New Roman، وبسطر مزدوج، على وجه واحد من ورق A4 (21.6 × 27.9 سم) مع حواشي 3.71 سم ، باستخدام معالج كلمات ميكروسوفت وورد 2000 أو ما اسْتَجَد منه. ويجري تنظيم أجزاء المخطوط وفق الترتيب التالي: صفحة العنوان، الملخص، رموز التصنيف (PACS)، المقدّمة، طرق البحث، النتائج، المناقشة، الخلاصة، الشكر والعرفان، المراجع، الجداول، قائمة بدليل الأشكال والصور والإيضاحات، ثَمَّ الأشكال والصور والإيضاحات. وتُكْتَب العناوين الرئيسة بخطٍّ **غامق**، بينما تُكْتَب العناوين الفرعية بخطٍّ *مائل*.

صفحة العنوان: وتشمل عنوان المقالة، أسماء الباحثين الكاملة وعناوين العمل كاملة. ويكتب الباحث المسؤول عن المراسلات اسمه مشارا إليه بنجمة، والبريد الإلكتروني الخاص به. ويجب أن يكون عنوان المقالة موجزا وواضحا ومعبرا عن فحوى (محتوى) المخطوط، وذلك لأهمية هذا العنوان لأغراض استرجاع المعلومات.

الملخص: المطلوب كتابة فقرة واحدة لا تزيد على مائتي كلمة، موضحة هدف البحث، والمنهج المتبع فيه والنتائج وأهم ما توصل إليه الباحثون.

الكلمات الدالة: يجب أن يلي الملخص قائمة من 4-6 كلمات دالة تعبر عن المحتوى الدقيق للمخطوط لأغراض الفهرسة.

PACS: يجب إرفاق الرموز التصنيفية، وهي متوافرة في الموقع http://www.aip.org/pacs/pacs06/pacs06-toc.html.

المقدمة: يجب أن توضّح الهدف من الدراسة وعلاقتها بالأعمال السابقة في المجال، لا أن تكون مراجعة مكثفة لما نشر (لا تزيد المقدمة عن صفحة ونصف الصفحة مطبوعة).

طرائق البحث (التجريبية / النظرية): يجب أن تكون هذه الطرائق موضحة بتفصيل كاف لإتاحة إعادة إجرائها بكفاءة، ولكن باختصار مناسب، حتى لا تكون تكرارا للطرائق المنشورة سابقا.

النتائج: يستحسن عرض النتائج على صورة جداول وأشكال حيثما أمكن، مع شرح قليل في النص ومن دون مناقشة تفصيلية.

Subscription Form

Jordan Journal of

PHYSICS

An International Peer-Reviewed Research Journal

Published by the Deanship of Research & Graduate Studies, Yarmouk University, Irbid, Jordan

Name: ..... الأسم:

Specialty: ..... التخصص:

Address: ..... العنوان:

P.O. Box: ..... صندوق البريد:

City & Postal Code: ..... المدينة/الرمز البريدي:

Country: ..... القطر:

Phone: ..... رقم الهاتف:

Fax No: ..... رقم الفاكس:

E-mail: ..... البريد الإلكتروني:

No. of Subscription: ..... عدد الإشتراكات:

Method of Payment: ..... طريقة الدفع:

Amount Enclosed: ..... المبلغ المرفق:

Signature: ..... التوقيع:

Cheques should be paid to Deanship of Research and Graduate Studies - Yarmouk University.

I would like to subscribe to the Journal

For

- ☐ One Year
- ☐ Two Years
- ☐ Three Years

One Year Subscription Rates

	Inside Jordan	Outside Jordan
Individuals	JD 8	€ 40
Students	JD 4	€ 20
Institutions	JD 12	€ 60

Correspondence

Subscriptions and Sales:

Prof. Ibrahim O. Abu-AlJarayesh
Deanship of Research and Graduate Studies
Yarmouk University
Irbid – Jordan
Telephone: 00 962 2 711111 Ext. 2096
Fax No.: 00 962 2 7211121

المملكة الأردنية الهاشمية

جامعة اليرموك

المجلة الأردنية
للفيزياء

مجلة بحوث علمية عالمية محكّمة

المجلد (3)، العدد (1)، 2010م / 1431هـ

المجلة الأردنية

للفيزياء

مجلة بحوث علمية عالمية محكّمة

المجلد (3)، العدد (1)، 2010م / 1431هـ

المجلة الأردنية للفيزياء: مجلة بحوث علمية عالمية محكّمة أسستها اللجنة العليا للبحث العلمي، وزارة التعليم العالي والبحث العلمي، الأردن، وتصدر عن عمادة البحث العلمي والدراسات العليا، جامعة اليرموك، إربد، الأردن.

ترسل البحوث إلى العنوان التالي:

الأستاذ الدكتور إبراهيم عثمان أبو الجرايش
رئيس تحرير المجلة الأردنية للفيزياء
عمادة البحث العلمي والدراسات العليا، جامعة اليرموك
إربد ، الأردن
هاتف 7211111 2 962 00 **فرعي** 3735
E-mail: *jjp@yu.edu.jo*
Website: *http://Journals.yu.edu.jo/jjp*